Laser powder bed fusion of TiB_2-modified Cu15Ni8Sn alloy: processability, microstructure and mechanical performance

Jian Gao[a], Quanquan Han[a*], Liqiao Wang[a*], Zhongyi Liu[a], Shwe Soe[b], Zhenhua Zhang[a], Yuchen Gu[c]

[a]Key Laboratory of High Efficiency and Clean Mechanical Manufacture of Ministry of Education, School of Mechanical Engineering, Shandong University, Jinan, 250061, China
[b]Department of Engineering, Design and Mathematics, University of the West of England, Bristol BS16 1QY, UK
[c]College of Engineering, Swansea University, Swansea SA1 8EN, UK

Corresponding author: Quanquan Han, hanquanquan@sdu.edu.cn
Liqiao Wang, wangliqiao@sdu.edu.cn

Abstract

Cu15Ni8Sn is widely used in the aerospace and electronics domains because of its good conductivity and toughness. Due to the material's high laser reflectivity and thermal conductivity, however, employing the laser powder bed fusion (LPBF) additive manufacturing process on Cu15Ni8Sn alloy has been a challenge. This issue was addressed in the present study by modifying the Cu15Ni8Sn powder by adding 1 wt.% submicrometre TiB_2 ceramic particles. The results indicate that the LPBF's processability was improved by the increased laser absorption rate caused by the addition of 1 wt.% TiB_2, which eliminated pores and unmelted area defects. The addition of 1 wt.% TiB_2 also improved the components' surface quality by reducing the surface roughness value of 39.3% compared to the original Cu15Ni8Sn. The findings also indicate that the added TiB_2 particles reduced Sn-segregation behaviour, implying that the content and size of the segregated phase could be tailored by the suitable selection of ceramic materials and LPBF process parameters. Another advantage lies in the enhancement of mechanical performance, where a 11% increase in yield strength and 14% increase in ultimate tensile strength were achieved in the LPBF-fabricated modified Cu15Ni8Sn material. In this study, the primary strengthening mechanisms for LPBF-fabricated original Cu15Ni8Sn

were found to include dislocation strengthening and grain boundary strengthening. Orowan precipitation strengthening also played a significant role in the Cu15Ni8Sn-1wt.% TiB_2 material, as did dislocation strengthening and grain boundary strengthening. These findings provide a promising strategy to improve the LPBF processability of the advanced copper-based materials used in several key fields.
Keywords: Cu15Ni8Sn alloy; laser powder bed fusion; additive manufacturing; processability; strengthening mechanisms

1. Introduction

As an advanced metal additive manufacturing technology, laser powder bed fusion (LPBF) can be used to selectively melt metal powder layer by layer through the use of a high-energy laser, which can theoretically be used to fabricate complex-shaped metallic components [1]. LPBF has shown great potential in manufacturing advanced engineering components for various domains. Due to the unique characteristics of rapid melting/non-equilibrium solidification, LPBF has also shown significant advantages in suppressing elemental segregation, refining microstructure and improving mechanical properties [2,3]. The LPBF process has been successfully applied to manufacture components of titanium-based [4,5], aluminum-based [6,7] and nickel-based [8–10] alloys. Compared to the above materials, copper alloys exhibit the high laser reflectivity and thermal conductivity, significantly reducing their LPBF processability. Despite these challenges, a few studies have reported the LPBF of copper alloys, including pure Cu [11], Cu-Cr series [12], Cu-Sn series [13] and Cu15Ni8Sn [14,15].

Cu15Ni8Sn has shown great potential in the aerospace, electronics domains because of its high strength, good corrosion resistance and excellent wear resistance [16]. Due to the high content of Sn, the traditional casting process, however, generate serious Sn macro-segregation in processing Cu15Ni8Sn

alloy [17,18]. Previous studies have revealed that the extremely high cooling rate (10^5~10^7 K/s [19]) of LPBF could effectively reduce the Sn segregation, refine grains and improve mechanical properties. Zhang et al. [14] investigated the microstructure and mechanical properties of Cu15Ni8Sn-0.2Nb prepared by LPBF; they found that the as-fabricated Cu15Ni8Sn showed the α-Cu matrix phase with Sn-enriched γ precipitated phase, and Sn segregation was greatly suppressed at micron-scale caused by rapid cooling rate. Li et al. [15] found that the LPBF-fabricated Cu15Ni8Sn was composed of periodic equiaxed and columnar grains, and this periodic microstructure showed a positive effect on the improvement of mechanical properties. It should be noted that the above published studies have mainly employed high-power lasers (e.g. 400 W and above) to fabricate the Cu15Ni8Sn material while the reflected laser may damage the galvanometer [20]. Also, the high-reflectivity challenge has not been addressed and the strengthening mechanisms of LPBF-fabricated Cu15Ni8Sn specimens have not been systematically investigated.

Recently, Liu et al. [21] uniformly adhered Co particles with low laser reflectivity to Cu powder by mechanical mixing, which reduced the laser reflectivity of pure copper and improved the LPBF processability and mechanical properties of pure copper. The authors did not reveal the laser reflectivity reduction mechanism, however. Other reports have also shown that the inclusion of other metal particles on the surface of copper material can reduce laser reflectivity [22,23]. Compared to Co and other metal particles, submicrometre-sized TiB_2 ceramic particles offer lower laser reflectivity and good chemical stability, conductivity and thermophysical properties [24], thus making the material applicable for the LPBF of aluminium-based and nickel-based alloys to improve their processability and mechanical properties [25–27]. An investigation of the effects of TiB_2 ceramic particles during the LPBF of Cu15Ni8Sn would thus be interesting in terms of laser reflectivity reduction, processability improvement and mechanical property enhancement.

In this context, the processability, microstructure and mechanical properties

of Cu15Ni8Sn modified by 1 wt.% submicron TiB_2 ceramic particles were systematically studied in the current work to reveal the influences of TiB_2 ceramic particles during the LPBF of Cu15Ni8Sn alloy. In addition, the strengthening mechanisms of LPBF-manufactured Cu15Ni8Sn-1wt.% TiB_2 and original Cu15Ni8Sn were also examined to understand the effects of the addition of TiB_2 on the LPBF-fabricated Cu15Ni8Sn material.

2. Materials and methods

2.1. Material preparation

The pure gas-atomized Cu15Ni8Sn powder (Vilory Corporation, Jiangsu, China) used in this study exhibited a good degree of sphericity (Fig. 1a). The particle size distribution was measured as the following: D10 = 21.7 μm, D50 = 35.0 μm and D90 = 55.1 μm (Fig. 1b). The chemical composition of the Cu15Ni8Sn powder was (wt.%) 14.96Ni-8.01Sn-Bal (Cu). This alloy is prone to the segregation of Sn, regardless of traditional casting and powder metallurgy, and the segregation may adversely affect the properties of this material [28]. An apparent Sn segregation was observed in the Cu15Ni8Sn power (Fig. 1c).

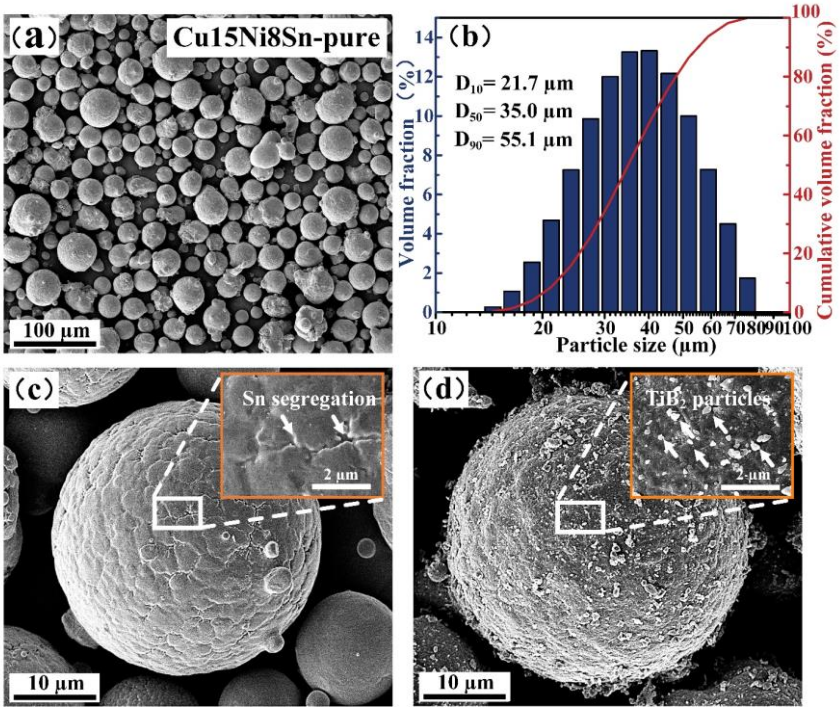

Fig. 1. Scanning electron microscopy (SEM) images of the powder materials used in this study: (a) Cu15Ni8Sn-pure powder; (b) Cu15Ni8Sn-pure powder particle size distribution; (c) high-magnification SEM image of a single Cu15Ni8Sn powder; (d) high-magnification SEM image of a single Cu15Ni8Sn-1wt.% TiB_2 powder.

The TiB_2 ceramic particles used in the study were at the submicron level, ranging from 100 nm to 900 nm in size, with an average particle size of 600 nm (CWnano Corp., Shanghai, China). The pure Cu15Ni8Sn powder and TiB_2 ceramic particles were mixed with a mass fraction ratio of 99:1. A commercial high-speed mixer (SpeedMixer DAC–800.1 FVZ, Nordrhein-Westfalen, Germany) was employed to synthesize the TiB_2-modified Cu15Ni8Sn feedstock (Cu15Ni8Sn-1wt.% TiB_2). The mixing parameters employed included a 1200 rpm mixing speed, with a total of 5 min of mixing time. To prevent overheating during the mixing process, the mixing procedure was to mix for 2.5 min, pause for 5 min, and then mix again for 2.5 min. As shown in Fig. 1d, the TiB_2 particles uniformly adhered to the surface of the Cu15Ni8Sn powder. Notably, the TiB_2 particles smoothed the grain boundary of the cellular crystal structure during the mixing process, which may have been beneficial for reducing the Sn segregation in the LPBF-fabricated modified Cu15Ni8Sn material.

2.2. Laser powder bed fusion (LPBF) process

Cu15Ni8Sn-pure and Cu15Ni8Sn-1wt.% TiB_2 samples were manufactured using Mlab cusing 200R (Concept Laser GmbH, Germany), equipped with a 200 W continuous wave fibre laser with a spot size of 75 μm. To prevent oxidation of the LPBF samples, the atmosphere of high-purity (99.99 wt.%) argon gas was maintained in the build chamber during the LPBF process. In this study, 6 x 6 x 7 mm^3 cubes of Cu15Ni8Sn-pure and Cu15Ni8Sn-1wt.% TiB_2 specimens were fabricated for parameter optimization. A maximum power of 190 W was adopted in this study. Given the high thermal gradient and residual stress generated within the rapid melting/solidification process, a chessboard scanning strategy was employed in the present study rather than a linear scanning strategy. A rotation angle of 67° was also used between two adjacent

layers to minimize any metallurgical defects or anisotropy of the LPBF samples [29]. The LPBF-processing parameters for optimization are listed in Table 1.

Table 1. Process parameters for laser powder bed fusion (LPBF) process optimization.

LPBF parameters	Value
Laser spot diameter	75 µm
Scanning strategy	chessboard
Rotation angle	67°
Laser power	190 W
Layer thickness	30 µm
Hatch spacing	100 µm
Scanning speeds	200, 250, 300, 350, 400, 450, 500, 550, 600 mm/s

The cube densities of the LPBF-fabricated Cu15Ni8Sn-pure and Cu15Ni8Sn-1wt.% TiB_2 specimens under different process parameters were determined by measuring the samples three times and averaging the values based on the Archimedes principle to determine the optimal parameters. Thermal conductivity samples (10 x 10 x 6 mm^3 cubes) and tensile samples of Cu15Ni8Sn-pure and Cu15Ni8Sn-1wt.% TiB_2 were then manufactured under their respective optimal conditions.

2.3. Materials characterization techniques

Both Cu15Ni8Sn-pure and Cu15Ni8Sn-1wt.%-TiB_2 modified samples were cut down along the XOY plane perpendicular to the build direction (Z axis) using the wire electrical discharge machining process. The section was then ground (with 320, 600 and 1500 mesh SiC sandpapers) and then polished (with 3 µm, 1µm diamond suspension, and finally 0.04 µm oxide polishing suspension colloidal silica). A laser scanning confocal microscope (VK-X200K, Keyence, Japan) was used to measure the 3D topography information of the top surface of the samples. The microstructures and defects distribution of these samples were characterized using optical microscopy (OM) and scanning electron microscopy (SEM). The percentage of defects area and the element Sn segregation area were both statistically measured using the ImageJ software.

The grain size distribution, grain boundary, dislocation, pole figure (PF) and inverse pole figure (IPF) of both materials were measured by electron backscatter diffraction (EBSD). The EBSD scanning voltage was set to 20 kV, the scanning area was set to 400 x 400 μm^2 and the step distance was set to 0.8 μm. A scanning electron microscope (JSM–7800F, JEOL, Japan) equipped with an Oxford EBSD probe (NordlysMax3, Oxford, UK) was used for microstructure characterization. The EBSD data were analyzed using HKL Channel 5 software. The phase composition was detected by an X-ray diffraction (XRD) instrument (SmartLab 3 kW, Japan) with Cu-Kα radiation set at 40 kV in the 2θ range from 20° to 100°, with a step size of 0.013° and a count time of 1 s per step.

2.4. Mechanical characterization techniques

Room-temperature hardness was tested by an HVS–1000a microhardness tester (Huayuzhongxin, Laizhou, China) with a 200 g load and an indentation time of 10 s. Five measurements were conducted and averaged to determine each material's Vickers microhardness. Tensile testing was carried out with an electronic universal testing machine (FBS–100KNW, FBS, Shenzhen, China) with a strain rate of $0.6 \times 10^{-3}\ s^{-1}$ at room temperature. Three tensile samples (pure Cu15Ni8Sn: P-v250, TiB_2-modified Cu15Ni8Sn: M-v250 and M-v550) were tested to obtain the yield strength (YS), ultimate tensile strength (UTS) and elongation at break. The tensile samples were set to flat dog-bone shaped, cutting from the as-built pure Cu15Ni8Sn and TiB_2-modified Cu15Ni8Sn by electrical discharge machining. The gage length, width, and thickness of the tensile samples were set to 28 mm, 2.8 mm and 1.7 mm, respectively. The nano-indentation experiments were performed at room temperature by using a NanoTest Vantage system (Micro Materials, UK). Six measurements were conducted and averaged for each material. A Vickers indentation head was selected (with a maximum load of 200 mN, a holding time of 10 s and an unloading time of 10 s) to obtain the Young's modulus of pure and TiB_2-modified

samples. The thermal conductivity, thermal diffusivity and specific heat at room temperature were analysed using a thermal conductivity instrument (LFA 1000, Linseis, Germany). LPBF-fabricated Cu15Ni8Sn-pure, Cu15Ni8Sn-1wt.% TiB_2 and TiB_2 powders were tested with a UV-Vis-NIR spectrophotometer (Cary 5000, Agilent, USA) to study their laser absorption properties.

3. Results

3.1. Relative density and defects

Fig. 2a shows the relationship between the relative density and the energy density of LPBF-fabricated Cu15Ni8Sn-pure and Cu15Ni8Sn-1wt.% TiB_2 materials. The definition of linear laser energy density may be found in previous reports [30,31].

Overall, the relative density of LPBF-fabricated Cu15Ni8Sn-pure increased with an increase in laser energy density. A maximum relative density of 99.06% was achieved when a 316.67 J/mm^3 energy density value with a laser scanning speed of 200 mm/s was employed. A 253.33 J/mm^3 laser energy density with a scanning speed of 250 mm/s also contributed a relatively high density of 99.04%. Because of the efficiency of LPBF manufacturing, the 253.33 J/mm^3 condition was selected as the optimum for manufacturing the tensile specimens in this study. Interestingly, the relative density of LPBF-fabricated Cu15Ni8Sn-1 wt.% TiB_2 material showed a decreasing trend with an increase in energy density. The optimal laser energy density and scanning speed values were determined to be 115 J/mm^3 and 550 mm/s. The modified Cu15Ni8Sn specimens were also manufactured and studied under the 253.33 J/mm^3 condition for comparison to reveal the effects of TiB_2 on microstructure evolution.

Fig. 2b shows the laser absorption rates of Cu15Ni8Sn-pure powder, TiB_2 powder, and Cu15Ni8Sn-1wt.% TiB_2 powder in this study at different wavelengths. The laser absorption rate of Cu15Ni8Sn powder at the 1080 nm

wavelength was only 53.56%, which means that nearly half the laser energy was reflected, resulting in poor LPBF processability. Notably, the laser absorption of the modified Cu15Ni8Sn powder increased significantly. Compared to the pure Cu15Ni8Sn powder (53.56%), the laser absorption rate of Cu15Ni8Sn-1wt.% TiB_2 powder was measured to be 79.34% at the 1080 nm wavelength, with a 25.78% increase. The higher energy input to the TiB_2-modified sample promoted the fluidity of the molten metal, thereby significantly reducing metallurgical defects such as pores and unmelted regions. Therefore, the highest relative density value of the modified Cu15Ni8Sn (99.4%) obtained in this study was higher than that of Cu15Ni8Sn-pure (99.04%), indicating that the added TiB_2 improved the material's processability by enhancing the powder bed's laser absorptivity.

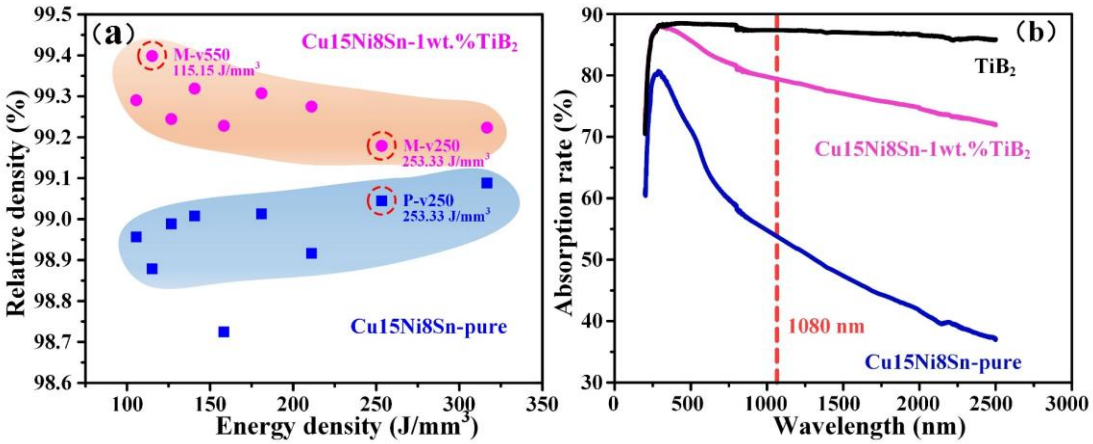

Fig. 2. Relative density and absorption rate: (a) Relative densities of Cu15Ni8Sn-pure and Cu15Ni8Sn-1wt.% TiB_2 at different laser energy density values; (b) Laser absorption rates for Cu15Ni8Sn-pure powder, TiB_2 powder, and Cu15Ni8Sn-1wt.% TiB_2 powder.

Fig. 3 shows the microstructure of the unetched LPBF-manufactured samples at the vertical sections (parallel to the build direction) under OM inspection. As shown in Fig. 3a, regular circular open pores and irregular unmelted areas with a size of over 200 μm were observed in the LPBF-fabricated pure Cu15Ni8Sn, even under the optimal condition. Under the same LPBF condition, defects were not detected in the TiB_2-modified Cu15Ni8Sn material, as shown in Fig. 3b. With an increase in scanning speed to the optimal value of 550 mm/s, the LPBF-fabricated TiB_2-modified Cu15Ni8Sn exhibited

nearly defect-free OM microstructure, indicating that the 1 wt.% TiB_2 addition significantly improved the LPBF processability of Cu15Ni8Sn.

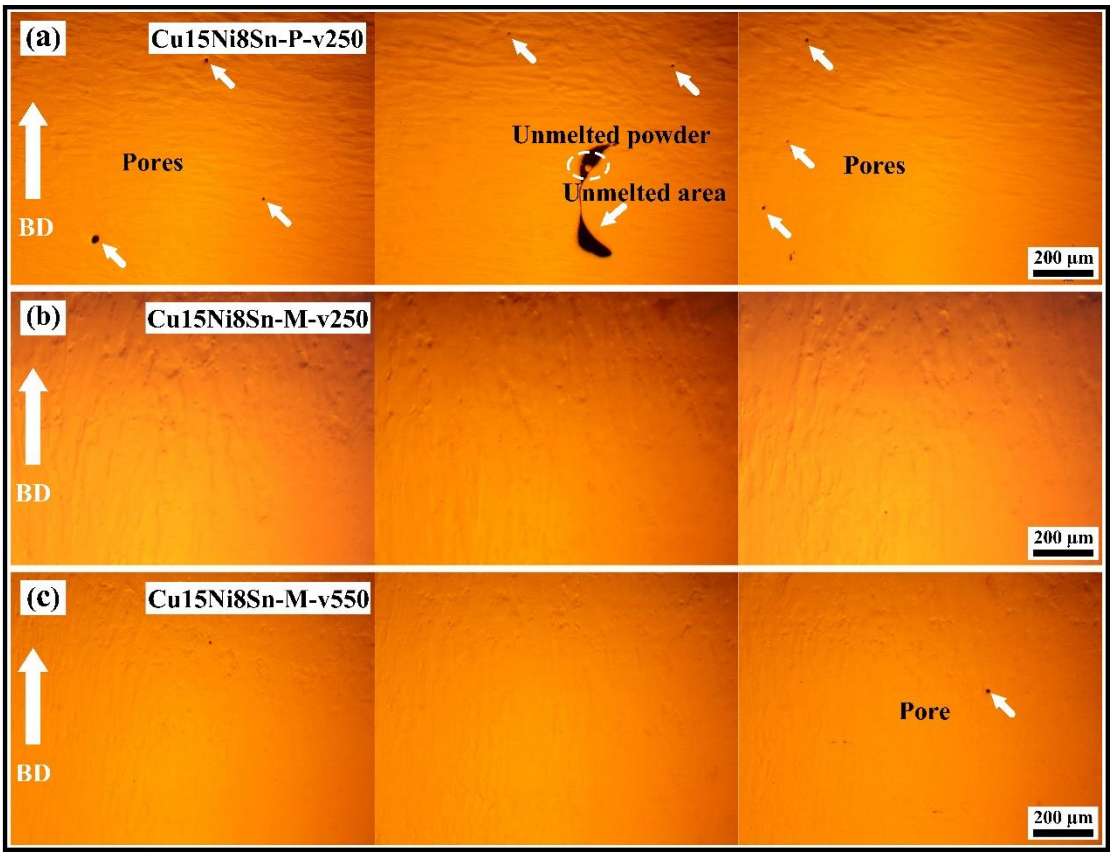

Fig. 3. Microstructure of unetched LPBF samples under optical microscopy (OM) along the build direction: (a) P-v250 with an optimal laser scanning speed of 250 mm/s; (b) M-v250 with a scanning speed of 250 mm/s; (c) M-v550 with a scanning speed of 550 mm/s.

Fig. 4 shows the OM microstructure of the three materials at the horizontal sections (perpendicular to the build direction). The defects area in the horizontal section was found to be much larger than that of the vertical section for the pure Cu15Ni8Sn material, where the defects area was calculated to be 2.48% (Fig. 4a), revealing poor LPBF processability for the Cu15Ni8Sn alloy. For the TiB_2-modified Cu15Ni8Sn materials, the OM microstructure at the horizontal sections was very consistent with that of the vertical sections (Fig. 4b–c), where a nearly defect-free microstructure was obtained. The addition of TiB_2 particles could reasonably be thought to have improved the laser absorptivity and further affected the Marangoni flow and the magnitude of capillary force within the LPBF process [2,32,33], thereby increasing the wettability of the solid-liquid

interface and significantly reducing defects.

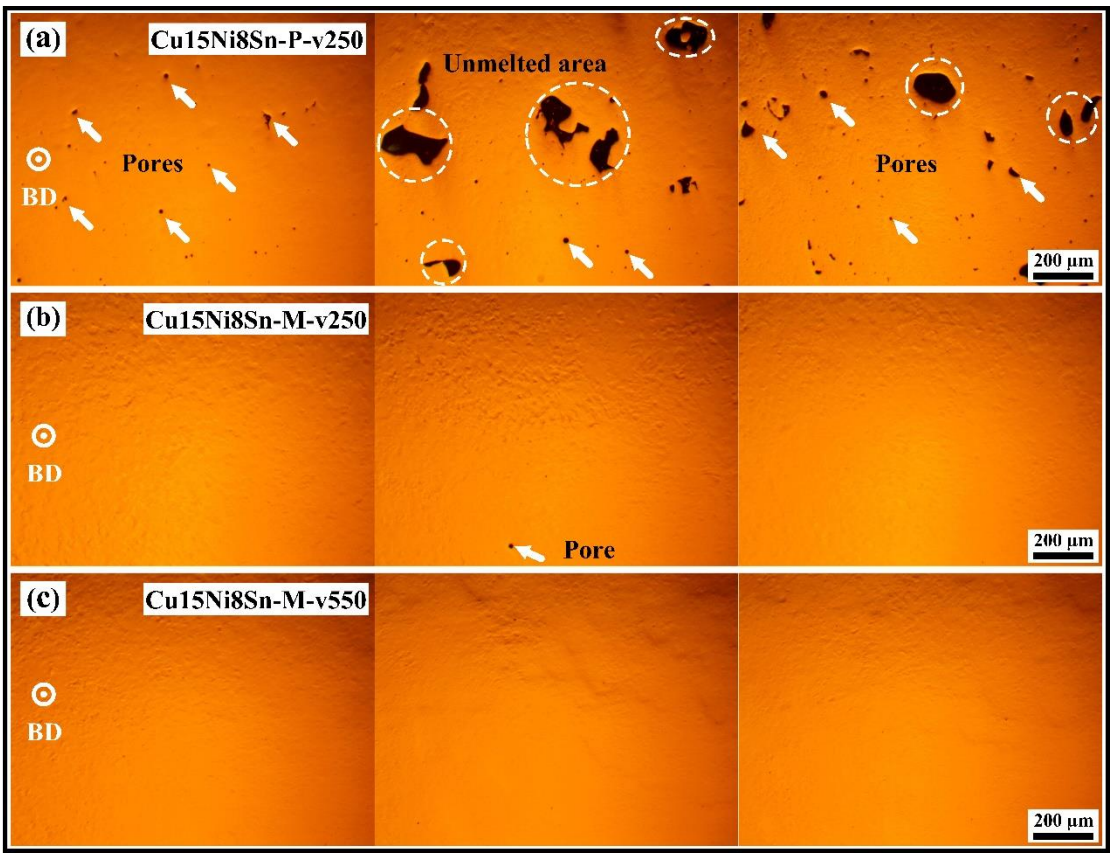

Fig. 4. Microstructure of unetched LPBF samples along the horizontal direction (perpendicular to the build direction): (a) P-v250; (b) M-v250; (c) M-v550.

3.2. Roughness

The surface roughness values at the top surface of the P-v250, M-v250 and M-v550 samples were measured and are illustrated in Fig. 5. The average area roughness of the LPBF-fabricated pure Cu15Ni8Sn was measured to be Sa = 13.46 μm, with clear melt pool patterns observed after rapid solidification (Fig. 5a/b). The relatively high surface roughness may be attributed to the poor processability of this material, caused by the high laser reflectivity. The insufficient energy input may have caused melt pool instability and the formation of unmelted-particles defects, thus leading to poor surface quality.

Due to the addition of TiB_2, and the laser reflectivity being reduced, more energy input allowed the TiB_2-modified samples (M-v550, M-v250) to affect the liquid pool, thus enhancing the fluidity of the molten metal. This step significantly reduced the defects caused by the spheroidization phenomenon

and improved the surface quality found in the roughness values of the M-v250 (Sa = 9.724 μm) and M-v550 (Sa = 8.085 μm) specimens by 27.76% and 39.93%, respectively (Fig. 5c–f). Note that the melt pool patterns after solidification were not as clear as for the pure Cu15Ni8Sn specimens. The findings indicate that the added TiB_2 particles smoothed the components' surface finishes by altering the melting/solidification process to some degree.

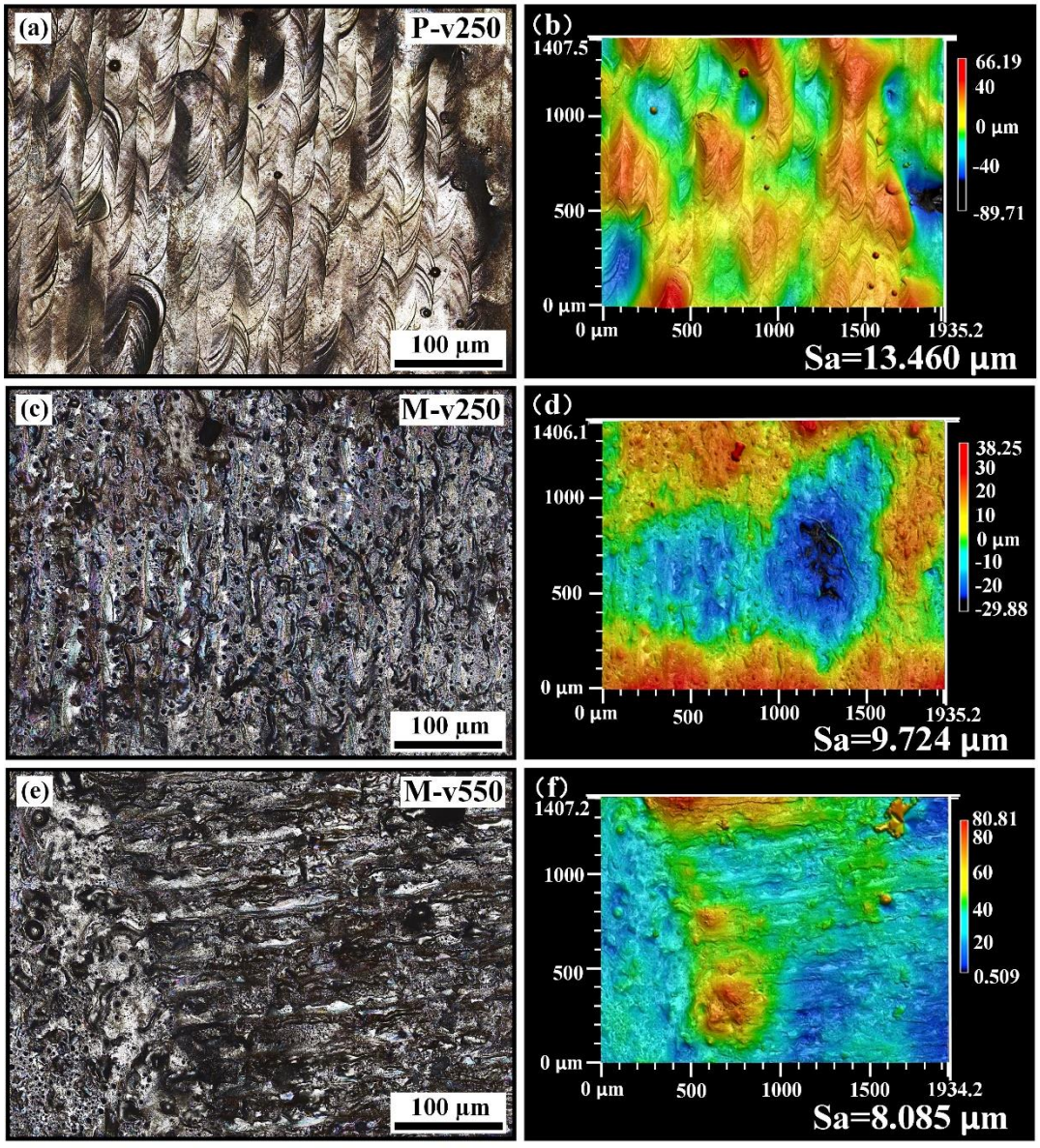

Fig. 5. Surface roughness of the LPBF-fabricated samples: (a) P-v250; (b) M-v250; (c) M-v550.

3.3. Phase and microstructure

The XRD patterns obtained from the P-v250 and M-v550 samples were examined in this study are shown in Fig. 6. Because the mass fraction of the

added TiB_2 was only 1wt.% and the size was at the submicron scale, the diffraction peaks of TiB_2 were not detected. Both samples exhibited the α-Cu primary phase (FCC) while the γ-$(CuNi)_3Sn$ phase was only detected in the pure sample; the 2θ values of γ-$(CuNi)_3Sn$ phase were measured to be 25.49°, 29.72°, 62.4° and 78.61°, respectively. The findings were consistent with the reported work [28] that the α-Cu phase is a Sn-depleted α-Cu(Ni,Sn) matrix, while the γ-$(CuNi)_3Sn$ is a Sn-enriched brittle phase. Interestingly, the typical diffraction peaks of the γ-$(CuNi)_3Sn$ phase were not detected in the M-v250 sample, probably because of the low content of the γ phase in the TiB_2 modified Cu15Ni8Sn material. A comparison of the XRD results between the pure and TiB_2-modified samples showed that the added TiB_2 contributed to the reduction of γ phase precipitation.

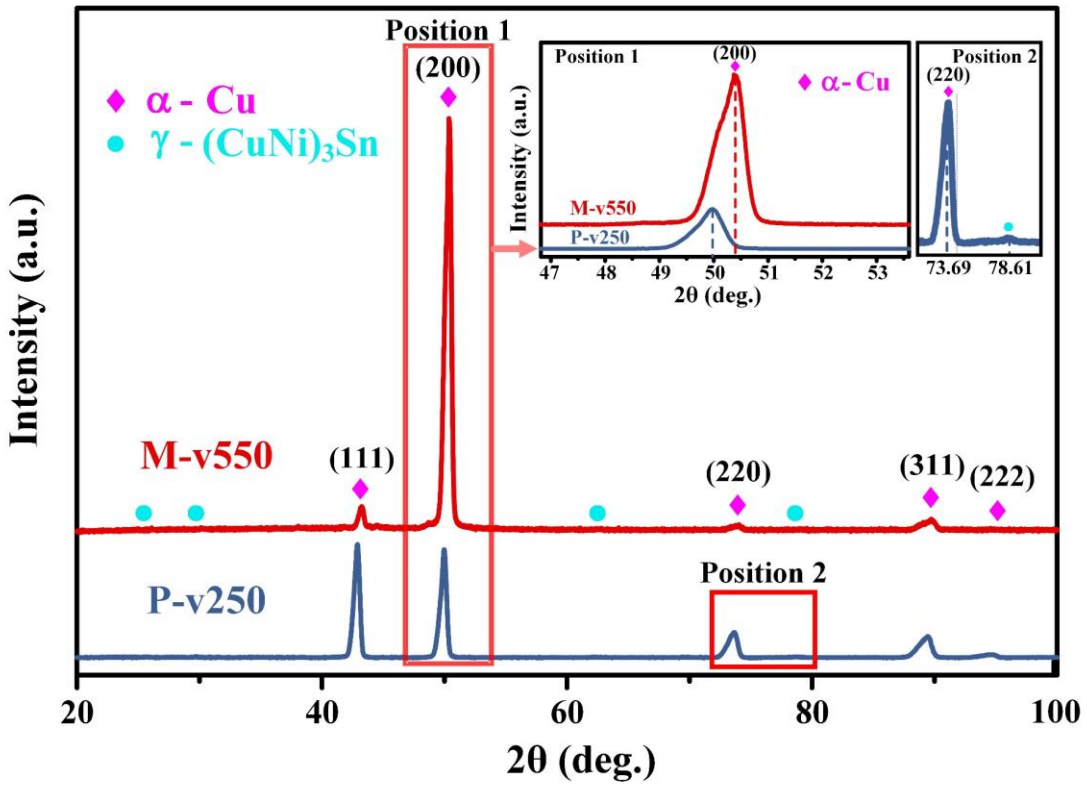

Fig. 6. X-ray diffraction (XRD) patterns of the LPBF-fabricated Cu15Ni8Sn-pure (P-v250) and Cu15Ni8Sn-1wt.% TiB_2 samples (M-v550).

On the basis of the XRD detection, no new phases formed or were detected in the LPBF-manufactured P-v250 and M-v550 materials. The diffraction peaks in the range of 2θ = 47°–53° were magnified to clearly show the change of the

(200) crystal plane diffraction peak of the two materials, while the diffraction peaks in the range of 2θ = 71°–80° were magnified to clearly show the γ-$(CuNi)_3Sn$ phase of pure sample. The 2θ values of the strong diffraction peak of the (200) crystal plane in the P-v250 and M-v550 samples were measured to be 49.98° and 50.37°, respectively. According to the Bragg's law [34], the right offset of the 2θ value indicated that the (200) crystal plane in the M-v250 had a relatively small interplanar spacing, possibly caused by residual stress and lattice distortion during LPBF non-equilibrium metallurgical processing [35]. Given the accuracy of XRD, further characterizations were conducted in this study to reveal the effects of the added TiB_2 particles on microstructural evolution in Cu15Ni8Sn.

Fig. 7 shows the microstructure of the LPBF-fabricated pure and TiB_2-modified Cu15Ni8Sn materials under SEM and EDX characterization. Sn segregation was noted in all three specimens after rapid solidification had occurred. The size of the segregated phase in the TiB_2-modified materials was also measured to be larger than that in the pure Cu15Ni8Sn (Fig. 7a–c). Energy-dispersive spectroscopy (EDS) mapping was performed on matrix (point 3 and point 6) and Sn segregation (point 2 and point 5), which further confirmed that the matrix was Sn-depleted α-Cu(Ni,Sn) phase and the Sn segregation was Sn-enriched γ-$(CuNi)_3Sn$ nano-precipitates phase. the Sn-segregation behaviour in the three materials and the uniformly distributed TiB_2 particles in the Cu matrix of the modified materials.

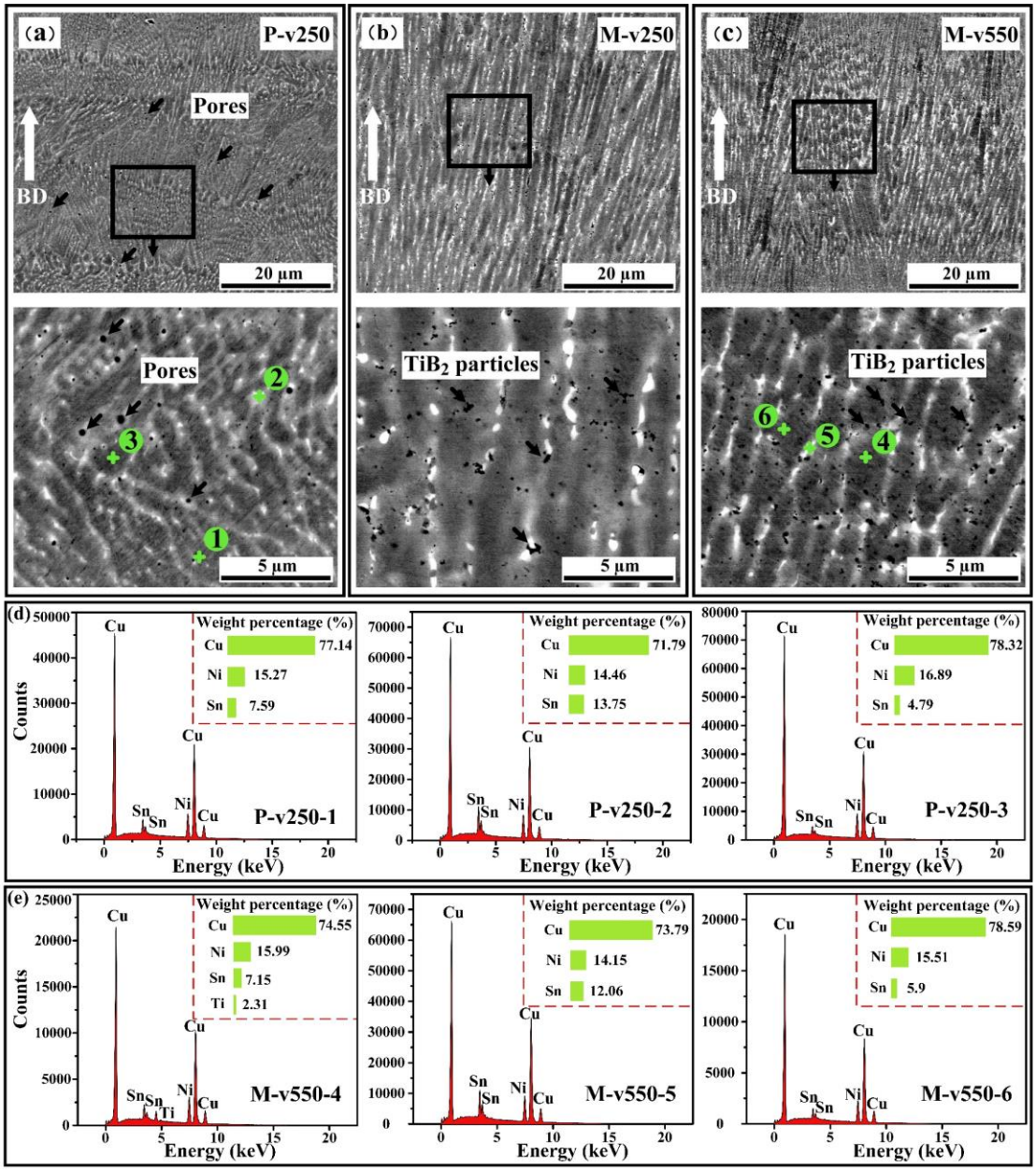

Fig. 7. Scanning electron microscopy (SEM) and energy-dispersive spectroscopy (EDS) images of Cu15Ni8Sn-pure and Cu15Ni8Sn-1wt.% TiB_2 samples: (a–c) low- and high-magnification SEM images of P-v250, M-v250 and M-v550; (d) EDS point scan of points 1, 2 and 3 in P-v250; (e) EDS point scan of points 4, 5 and 6 in M-v550.

EDS mapping also confirmed the uniformly distributed TiB_2 particles in the Cu matrix of the modified materials (Fig. 7d–e). On the basis of semi-quantitative EDS analysis and the average value of three SEM images through ImageJ calculations, the percentages of γ precipitates in P-v250, M-v250 and M-v550 were determined to be 5.75%, 4.94% and 5.29%, respectively. The size of γ precipitates in P-v250, M-v250 and M-v550 were determined to be 167.5

nm, 216.6 nm and 205.9 nm, respectively. Note that the γ phase formed at the grain and subgrain boundaries (the white phase observed in the Fig. 7a–c). Li et al. [15] also detected the γ phase formed in the LPBF-fabricated pure Cu15Ni8Sn material. The authors found that the grain refinement was strongly related to the Sn-enriched γ nano-precipitates phase and their distribution along the melt pool boundaries. Notably, the size of the added TiB_2 particles was reduced in the LPBF-fabricated specimens compared to the raw powder, implying that the TiB_2 particles may have partially melted in the melt pools under the strong laser irradiation. The addition of TiB_2 particles could conceivably reduce the Sn-segregation behaviour, and the size of the segregated phase could be tailored by the suitable selection of LPBF-process parameters.

The images in Fig. 8a–f show the grain orientations of the LPBF-fabricated Cu15Ni8Sn-pure and Cu15Ni8Sn-1wt.% TiB_2 samples obtained by EBSD examination. Very fine grains with a number of equiaxed grains were found to have formed in the pure Cu15Ni8Sn; ultrafine equiaxed grains tended to form along the fusion boundaries (Fig. 8a). This situation may be explained by the fact that the cooling rate at the melt pool boundary is generally higher than that of the other zones during the LPBF of single metallic materials [36]. This equiaxed-columnar bimodal grain structure is also known as a heterogeneous grain structure [15,21].

The P-v250 sample showed no apparent crystal orientation at the vertical section. Interestingly, the addition of TiB_2 particles did not appear to function as a heterogeneous nucleation site to promote grain refinement in the LPBF of the modified materials (Fig. 8b–c), while this behaviour has been widely reported in the LPBF of aluminium and nickel alloys [27,37–39]. More typical columnar grains formed in both the M-v250 and M-v550 specimens. Considering the layer thickness of 30 μm used in the present study, many columnar grains in M-v250 crossed over 10 layers (Fig. 8b/e), indicating that under the same LPBF condition, the added TiB_2 promoted the formation of columnar grains, probably by affecting the melt pool solidification behaviour. The strong thermal resistance

offered by the TiB_2 particles reduced the melt pool cooling rate and increased the thermal gradients, resulting in columnar grain growth. Under the optimal LPBF condition, the M-v550 material exhibited much finer grain structures compared to M-v250 due to the increased scanning speed (Fig. 8c/f). The equivalent diameters of P-v250, M-v250 and M-v550 were determined to be 4.9 μm, 7.48 μm and 7 μm, respectively.

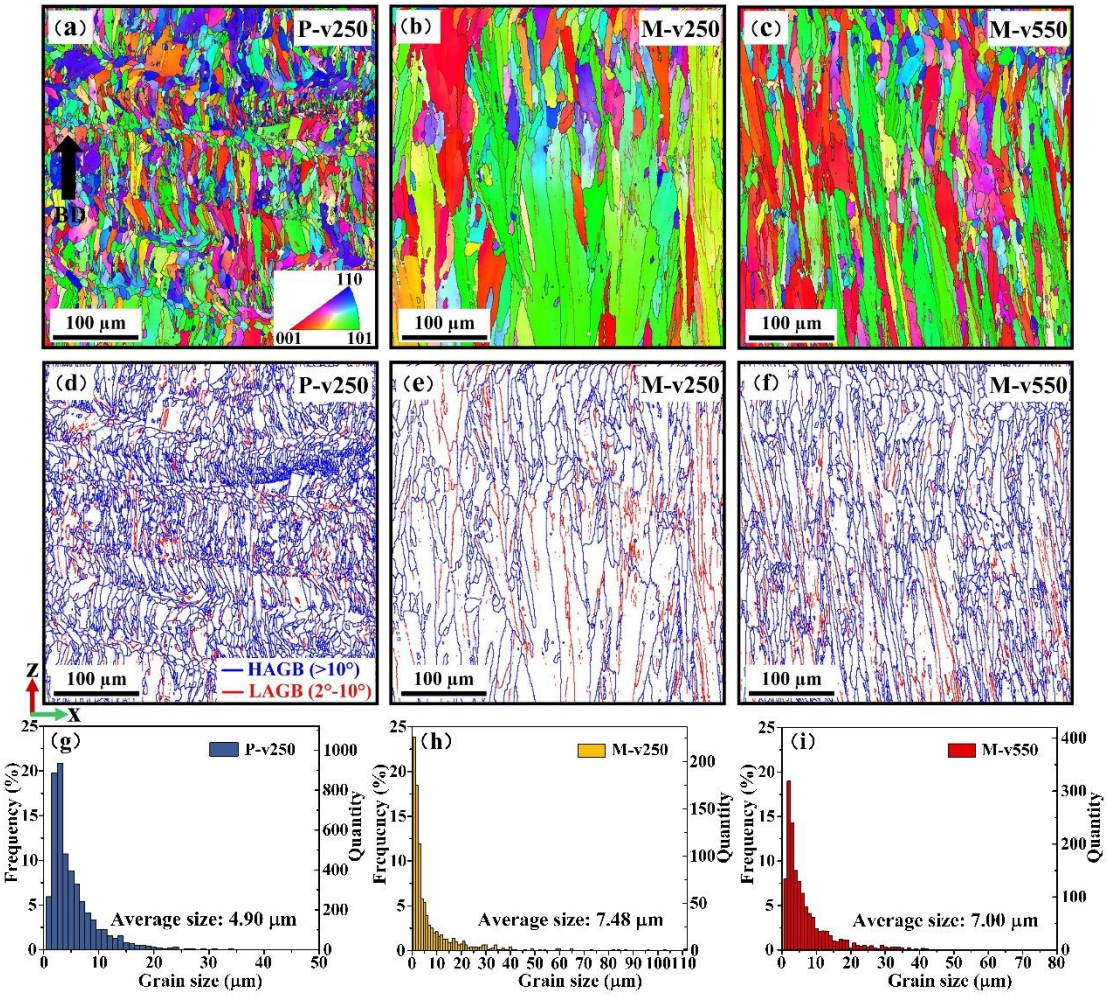

Fig. 8. Electron backscattered diffraction (EBSD) images of Cu15Ni8Sn-pure and Cu15Ni8Sn-1wt.% TiB_2 samples: (a–c) inverse pole figure (IPF) orientation map for P-v250, M-v250 and M-v550; (d–e) EBSD image quality map with high- and low-angle grain boundaries (HAGBs and LAGBs) superimposed for P-v250, M-v250 and M-v550; (g–i) EBSD image quality map showing the average grain size and fraction for the three materials.

It is worth noting that in general, the addition of TiB_2 changes the grain morphology, size and orientation of Cu15Ni8Sn alloy. The grain structures of the M-v250 and M-v550 samples are dominated by columnar grains. In contrast to the random crystal orientation of the P-v250 sample, both the M-v250 and

M-v550 samples exhibited a strong <101> crystal orientation. Related studies have shown that this behaviour may have been related to the internal stress and storage energy of the material [40]. The added TiB_2 particles improved the LPBF processability of Cu15Ni8Sn by minimizing the defects, but the inclusion also promoted the formation of columnar grains, which implies that grain refinement may not have been an influential factor in altering the mechanical performance of the modified Cu15Ni8Sn material. Investigating the changes of the added TiB_2 particles to the modified material would be an interesting course of study.

Fig. 9 shows the local misorientation maps and frequencies of the local misorientation angle (also known as the kernel average misorientation, or KAM) of the original Cu15Ni8Sn and TiB_2-modified Cu15Ni8Sn materials. The KAM is generally used to calculate the geometrically necessary dislocations (GNDs), correlated linearly with the magnitude of local plastic strain [41]. The GNDs were caused by the high thermal stress and strain in the LPBF-fabricated samples [42,43]. The P-v250 sample was found to have more GNDs than the M-v250 and M-v550 samples (Fig. 9a–c). The equivalent density of GNDs can be determined by $\rho^{GND} = 2KAM_{\text{ave}} / \mu b$ [44], where KAM_{ave} is the average KAM value of the tested region (also the average θ of the local misorientation in the selected region), μ is the step distance used for the EBSD (0.8 μm) and b is the Burgers vector (0.2556 nm) [45]. The average dislocation density values of the GNDs of the P-v250, M-v250 and M-v550 were determined to be 6.38×10^{14} m^{-2}, 5.61×10^{14} m^{-2} and 5.71×10^{14} m^{-2}, respectively (Fig. 9d–f). The variation of LPBF process parameters played a significant role in the GND density. When other process parameters were fixed, a higher laser scanning speed (v550) generally resulted in higher cooling rates, thermal gradients, and GND density compared to lower scanning speed conditions [56,57]. Note that the calculated dislocation density of the modified-Cu15Ni8Sn was slightly lower than that of the pure Cu15Ni8Sn, which was due to the presence of many dislocations and

dislocation tangles in the Cu15Ni8Sn-pure samples fabricated via LPBF, probably caused by the Sn segregation [28]. The SEM and EDS analyses (Fig. 7) also confirmed that the Sn segregation in the TiB_2-modified samples was lower than in the pure sample, resulting in a lower dislocation density in the TiB_2-modified sample.

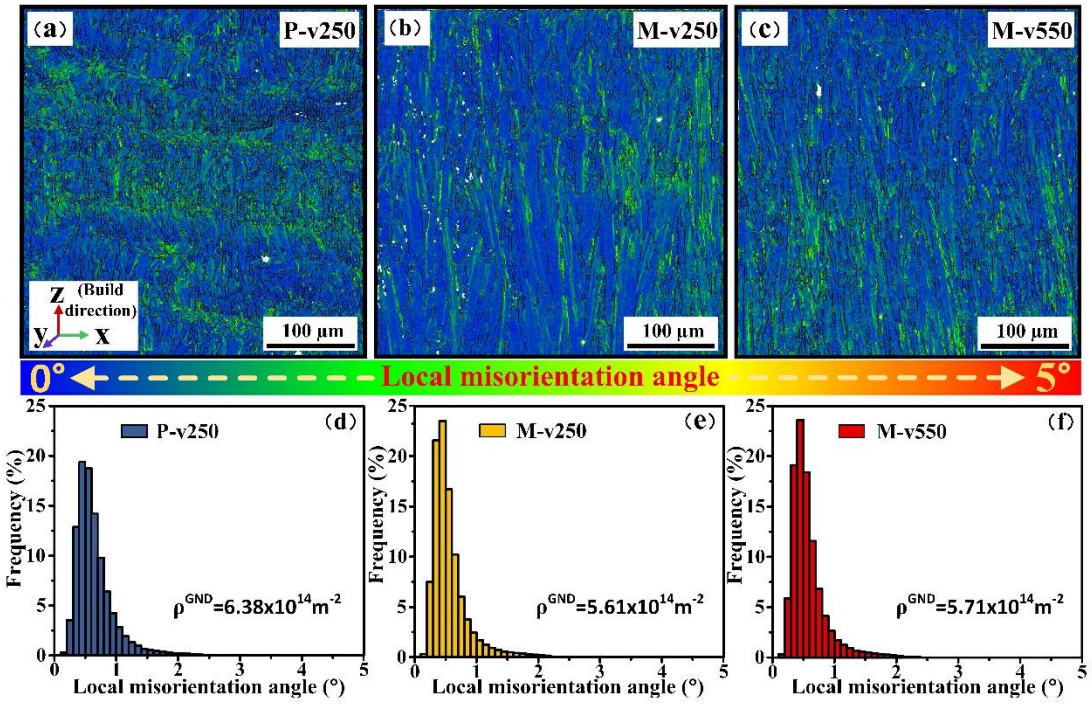

Fig. 9. Local misorientation maps of Cu15Ni8Sn-pure and Cu15Ni8Sn-1wt.% TiB_2 samples: (a–c) P-v250, M-v250 and M-v550; (d–f) frequency of the local misorientation angle map for P-v250, M-v250 and M-v550, respectively.

Fig. 10 shows the pole figures and inverse pole figures of the P-v250, M-v250 and M-v550 samples, measured at the vertical sections. Compared to the {110} and {111} textures, all three samples offered the highest maximum intensity of multiples of uniform density (MUD) in the {100} texture, determined to be 2.88, 11.44 and 10.06, respectively. Noticeably, the TiB_2-modified samples exhibited strong {100}, {110} and {111} textures, while the {110} and {111} textures were significantly weakened in the pure sample. Generally, the texture intensity is strongly linked to the LPBF-processing parameters and the material properties. This finding indicates that the added TiB_2 particles promoted the strong {100} texture (Fig. 10a/c/e). Combined with the IPF results, it reveals that the majority of the columnar grains of the TiB_2-modified samples offered preferred <100>

orientation parallel to the build direction. The typical fibre texture formed in the TiB_2-modified materials (M-v250 and M-v550) might be due to the high thermal gradients along the build direction [48,49]. Copper alloys are well known to have Bragg lattices with a face-centred cubic (FCC) structure. Compared with the {100} texture, the {110} and {111} textures are more important in FCC-based metal materials, which offer a better combination of strength and ductility [50,51]. The TiB_2-modified Cu15Ni8Sn materials fabricated via LPBF were thus expected to exhibit better tensile properties.

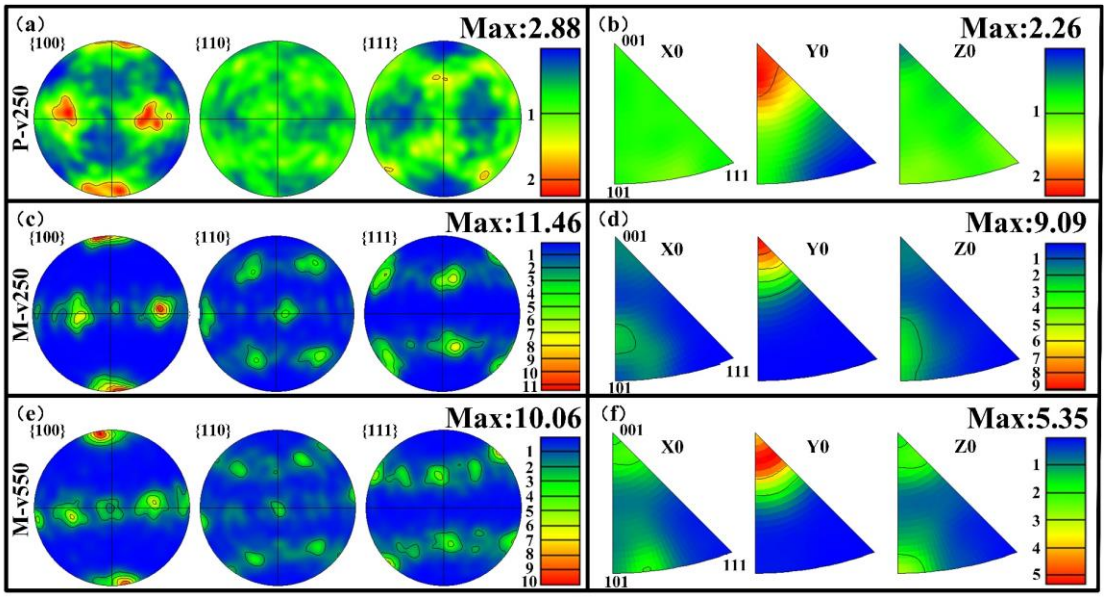

Fig. 10. Pole figures and inverse pole figures of Cu15Ni8Sn-pure and Cu15Ni8Sn-1wt.% TiB_2 samples: (a, c, e) PFs for P-v250, M-v250 and M-v550; (b, d, f) IPFs for P-v250, M-v250 and M-v550.

The texture strength in the inverse pole figure is also measured by the MUD indicator. The MUDs of the P-v250, M-v250 and M-v550 samples were determined to be 2.26, 9.09 and 5.35, respectively (Fig. 10b/d/f). This confirmed that the <100>//Y0 texture of the three materials was strong, and the <100> textures of the TiB_2-modified materials were stronger than that of the pure material. Previous studies have also reported that the {100} texture orientation is the preferential grain-growth orientation of FCC-based metal materials [31,52].

3.4. Mechanical properties

The tensile properties of both the LPBF-fabricated pure Cu15Ni8Sn and 1wt.% TiB_2-modified Cu15Ni8Sn samples were measured via uniaxial tensile testing at room temperature. The tensile engineering stress-strain curves are shown in Fig. 11a, as are the dimensions of the tensile samples. The yield strength (YS), ultimate tensile strength (UTS) and elongation at break (ε) values of the Cu15Ni8Sn-pure sample (P-v250) were determined to be 402 MPa, 524 MPa and 21.5%, respectively. Compared to the pure Cu15Ni8Sn, the 1wt.% submicrometre TiB_2-modified Cu15Ni8Sn exhibited higher strength. The YS and UTS values of the Cu15Ni8Sn-1wt.% TiB_2 sample (M-v550) were determined to be 448 MPa and 601 MPa, with an increase of 11.44% and 14.69%, respectively. The elongation at break in the M-v550 was found to be 17.8%, which was slightly lower than that of the P-v250 (21.5%). This increased strength may be attributed to the elimination of the defects (pores and unmelted areas) and the strengthening of the added 1wt.% TiB_2 ceramic particles. The YS, UTS and ε values of the LPBF-fabricated pure Cu15Ni8Sn and TiB_2-modified Cu15Ni8Sn materials are summarized in Table 2. Given the integral benefits of the combination of strength and ductility, the TiB_2-modified Cu15Ni8Sn showed better mechanical performance, which was also confirmed by our EBSD-based finding that strong {110} and {111} textures had formed in the TiB_2-modified specimens (Fig. 10). Considering the residual thermal stresses, metallurgical defects formed in the LPBF-fabricated components, the necessary post-heat treatments are required in order to further improve the mechanical performance and microstructure uniformity to meet the engineering standards. Previous studies [45,53,54] have revealed that the heat treatment employed is to produce spinodal decomposition and ordered precipitation phases to achieve excellent mechanical properties for the Cu15Ni8Sn alloy. Future work may study the effects of the solid solution and aging treatment on the LPBF-fabricated TiB_2-modified Cu15Ni8Sn materials. The strengthening

mechanisms of the three LPBF-fabricated materials are discussed in the next section.

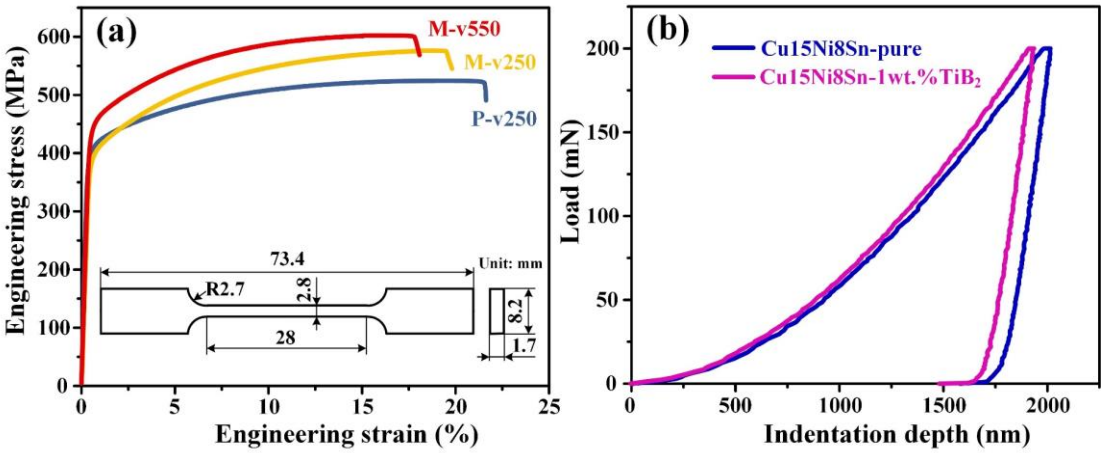

Fig. 11. Mechanical performance of the specimens: (a) engineering stress-strain curves; (b) nano-indentation load-indentation depth curves of Cu15Ni8Sn-pure (P-v250) and Cu15Ni8Sn-1wt.% TiB_2 samples (M-v250 and M-v550).

Fig. 11b shows the nano-indentation performance measured on the polished sections of the LPBF-fabricated pure Cu15Ni8Sn and TiB_2-modified Cu15Ni8Sn materials. The nano-indentation load-depth curves include three stages: loading, holding at maximum load and unloading. The initial slope and indentation depth of the unloading stage can be used to calculate the Young's modulus and nanohardness of the material. The Young's modulus and microhardness values for all three samples are also summarized in Table 2. Compared to the value for P-v250 (183 ± 6 HV0.2), the microhardness values of the two TiB_2-modified Cu15Ni8Sn specimens were found to have increased by 16.39% and 21.31%, respectively. The Young's modulus values of the pure Cu15Ni8Sn material and Cu15Ni8Sn-1wt.% TiB_2 material were measured to be 89.93 ± 1.82 GPa and 96.51 ± 1.46 GPa, respectively.

Table 2. Mechanical properties of Cu15Ni8Sn-pure (P-v250) and Cu15Ni8Sn-1wt.% TiB_2 samples (M-v250 and M-v550) via LPBF.

Samples	YS (MPa)	UTS (MPa)	ε (%)	Young's modulus (GPa)	Microhardness ($HV_{0.2}$)
P-v250	402	524	21.5	89.93 ± 1.82	183 ± 6
M-v250	396	575	19.5	96.51 ± 1.46	213 ± 3
M-V550	448	601	17.8	—	222 ± 8

Fig. 12 shows typical SEM fractographies of the fracture surfaces of all three specimens after tensile testing. The fracture surface of the original Cu15Ni8Sn specimen (P-v250) displayed relatively flat surfaces with a few metallurgical defects, including microscale pores and unmelted defects with a maximum size of 200 μm (Fig. 12a_1–a_2). Metallurgical defects were also observed in the as-fabricated pure Cu15Ni8n specimens (Figs. 3–4). Better metallurgical bonding formed in the TiB_2-modified specimens compared to the pure Cu15Ni8Sn alloy. A few cracks (about 100 μm in length) on the fracture surface, however, were observed in the M-v550 specimen (Fig. 12c_2). Fine and uniform dimples were observed from the high-magnification SEM images (Fig. 12a_3/b_3/c_3), indicating that all the specimens may have displayed typical ductile fracturing. Interestingly, uniformly distributed nanometre-scale particles in the fine dimples were detected in the TiB_2-modified specimens (Fig. 12b_3/c_3). Due to the uneven surface of the fracture, the chemical composition of the nanoscale particles was not detected under EDS analysis. Considering the uniform distribution and hexagonal prismatically shaped particles combined with the EDS point scan results (Fig. 7), we may reasonably infer that these particles were the added 1wt.% TiB_2 particles. The average dimple sizes of the original Cu15Ni8Sn (P-v250) and TiB_2-modified Cu15Ni8Sn (M-v250 and M-v550) materials were determined to be 445 nm, 654 nm and 589 nm, respectively. The size of the ductile dimples in the pure Cu15Ni8Sn specimen was smaller and deeper than that of the TiB_2-modified specimens, implying that the pure specimen offered better ductility. These fractographic observations are consistent with the mechanical properties obtained in the study (Fig. 11).

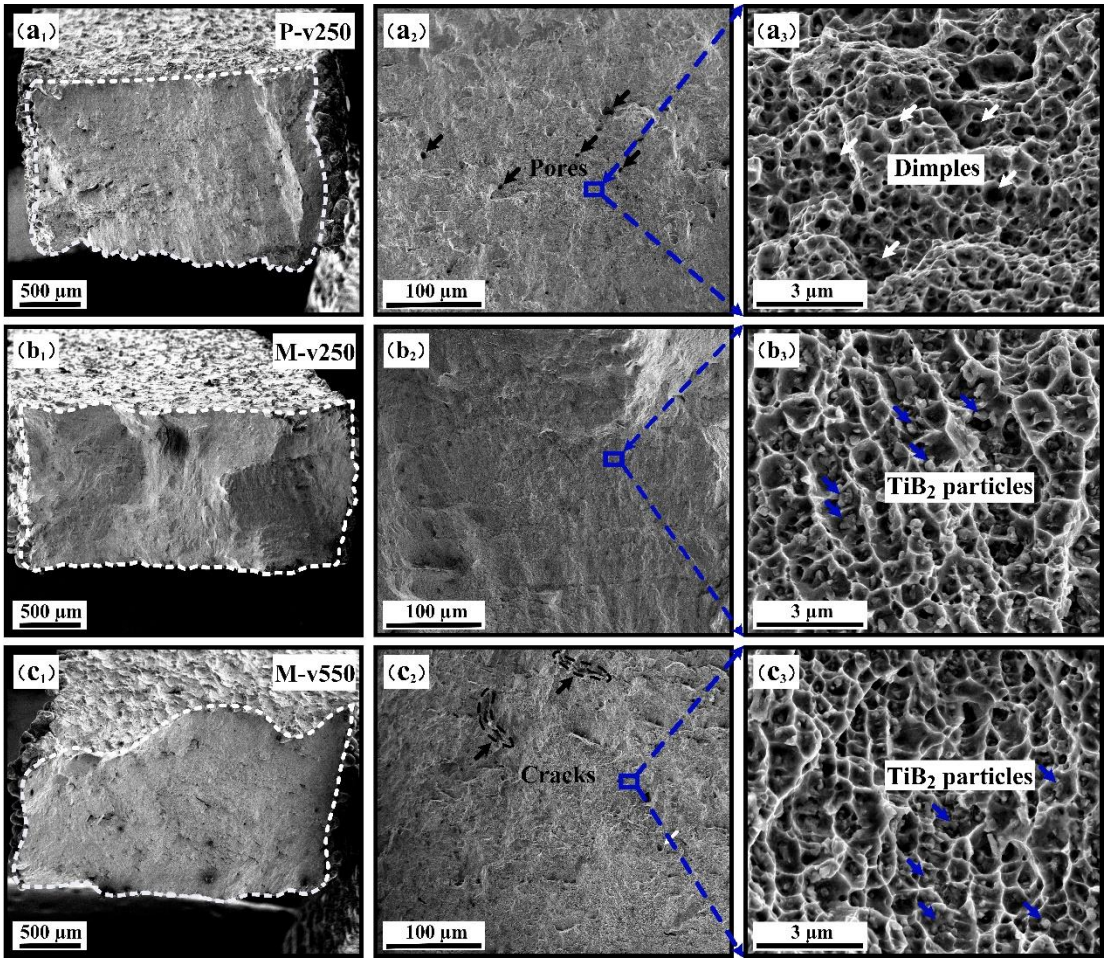

Fig. 12. SEM fractographies showing the fracture surfaces of Cu15Ni8Sn-pure and Cu15Ni8Sn-1wt.% TiB_2 specimens: (a_1–a_3) pure Cu15Ni8Sn specimen, P-v250; (b_1–b_3) TiB_2-modified Cu15Ni8Sn specimen, M-v250; (c_1–c_3) TiB_2-modified Cu15Ni8Sn specimen, M-v550.

4. Discussion

4.1 Effects of TiB_2 on thermophysical properties

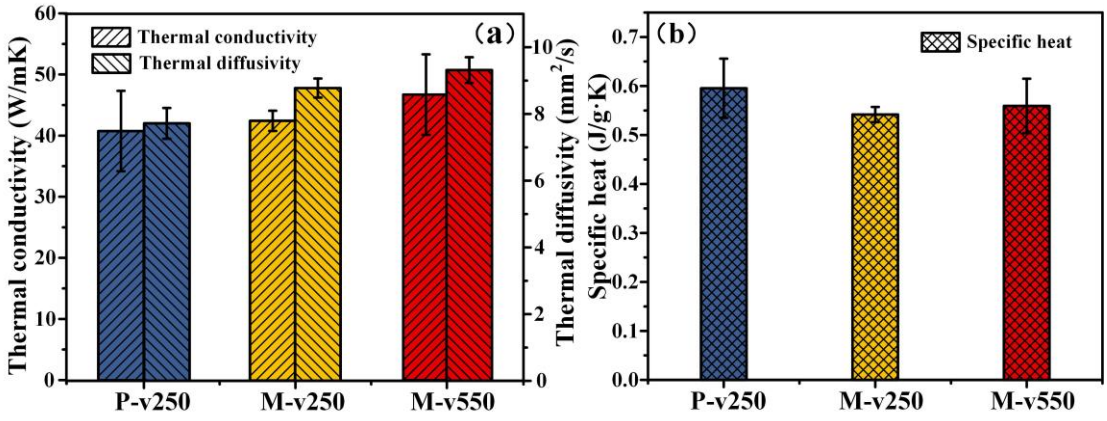

Fig. 13. Thermophysical properties of Cu15Ni8Sn-pure and Cu15Ni8Sn-1wt.% TiB_2 materials at room temperature: (a) thermal conductivities and thermal diffusivities, (b) specific heats for

P-v250, M-v250 and M-v550, respectively.

In general, the thermophysical properties and the laser absorptivity are the primary factors that affect the LPBF processability. The images in Fig. 13 show the thermophysical properties of Cu15Ni8Sn-pure and Cu15Ni8Sn-1wt.% TiB_2 samples at room temperature, including thermal conductivity, specific heat capacity and thermal diffusivity. Previous studies have demonstrated that the thermophysical properties of metals are mainly affected by porosity [55]. Due to the existence of fewer metallurgical defects and the higher density of the TiB_2-modified samples, and the fact that the added TiB_2 also has a high thermal conductivity [56], the modified Cu15Ni8Sn displayed higher thermal conductivity and thermal diffusivity than pure Cu15Ni8Sn. This finding indicates that the TiB_2 modified Cu15Ni8Sn material may disperse heat energy more efficiently compared to pure Cu15Ni8Sn when used in the cooling systems. The specific heat capacity of the M-v250 and M-v550 samples was examined to be a bit lower than that of the P-v250 sample. Second, studies have also shown that the thermal physical properties of metals are also affected by the precipitates and grain boundary fraction [57]. Interestingly, the TiB_2 modified samples showed different thermophysical properties and this could be due to the increase in density caused by the microstructural evolution. That is, the fraction of the α-Cu phase and precipitates in M-v550 was higher than that of M-v250.

4.2. Possible strengthening mechanisms

On the basis of the systematic microstructure characterization by XRD, SEM and EBSD, the LPBF-fabricated Cu15Ni8Sn-pure and Cu15Ni8Sn-1wt.% TiB_2 specimens offered different microstructure performances, which also resulted in differences in mechanical behaviour. As noted in the literature [15,58,59], the difference in mechanical performance may be attributed to the various strengthening mechanisms in the three materials.

Table 3. The terms used in this study.

Symbol	Description	P-v250	M-v250	M-v550	Reference
σ_0	Lattice friction of stress of Cu		52 MPa		[60]
k	Strengthening coefficient related to the grain boundary structure of Cu		0.356 MPa $m^{-1/2}$		[58]
d	Average grain size	/	/	/	This work
M	Taylor factor	/	/	/	This work
α	Proportionality coefficient of Cu		0.3		[58]
G	Shear modulus of this alloy	/		/	This work
b	Burgers vector of Cu		0.2556 nm		[45]
ρ	Dislocation density	/	/	/	This work
d_p	Average radius of the precipitate	/	/	/	This work
γ	Poisson's ratio of Cu		0.34		[61]
f_v	Volume fraction of precipitate	/	/	/	This work

4.2.1. Grain boundary strengthening

Generally, the extremely high cooling rate within the LPBF could have increased the grain boundary density by refining grains, and the increased grain boundaries could have strengthened the material by hindering the movement of dislocations. The contribution of grain boundary strengthening may be calculated by using the Hall–Petch formula [45,60]:

$$\sigma_{GBS} = k\mathrm{d}^{-\frac{1}{2}} \quad (1)$$

where k is a constant (the value of 0.356 MPa $m^{-1/2}$ from the literature was adopted in the present study [58]), and d is the grain size of the matrix. Based on Eq. (1), the contributions of grain boundary strengthening for the P-v250, M-v250 and M-v550 specimens were determined to be 160.8 MPa, 130.2 MPa and 134.6 MPa, respectively.

4.2.2. Dislocation strengthening

Dislocation strengthening can be estimated by the Bailey–Hirsch relation [62]:

$$\sigma_{DIS} = M\alpha Gb\sqrt{\rho} \quad (2)$$

where M is the Taylor factor, which was obtained from the EBSD measurement in this study; M is 3.10 for P-v250, 2.53 for M-v250 and 3.03 for M-v550; b is the Berger vector (0.2556 nm [45]); α is the geometric constant (α = 0.3 [58]); and G is the shear modulus, which is calculated from the following equation:

$$G = \frac{E}{2(1+\nu)} \quad (3)$$

where E is the Young 's modulus, ν is the Poisson 's ratio. Thus, the contributions of dislocation strengthening in the P-v250, M-v250 and M-v550 specimens were determined to be 361.7 MPa, 297.1 MPa and 358.9 MPa, respectively.

4.2.3. Orowan precipitation strengthening

As a precipitation hardening alloy, the δ precipitation ($(Cu_xNi_{1-x})_3Sn$) was uniformly distributed in the matrix, thus playing a significant role in hindering dislocation movement [15]. In addition, in contrast to the pure Cu15Ni8Sn sample, the added TiB_2 ceramic particles functioned as a second phase, which also hindered dislocation movement. The Orowan precipitation strengthening can be expressed by the Orowan–Ashby equation [63]:

$$\sigma_{ops} = 0.81\frac{MGb}{2\pi(1-\nu)^{1/2}}\frac{\ln(d_p/b)}{\lambda - d_p} \quad (4)$$

where λ is the spacing between the precipitates in the sliding plane. λ is related to the average diameter d_p and the volume fraction f_v of the precipitates and with the following equation [64]:

$$\lambda = \frac{1}{2}d_p\sqrt{\frac{3\pi}{2f_v}} \quad (5)$$

For the pure Cu15Ni8Sn sample (P-v250) and TiB_2-modified Cu15Ni8Sn

samples (M-v250 and M-v550)，the average d_p of the γ precipitates was calculated to be 167.5 nm, 216.6 nm and 205.9 nm，respectively, as shown in the SEM observation (Fig. 7). The volume fraction f_v of the γ precipitates was calculated to be 5.75 vol%, 4.94 vol% and 5.29 vol%, respectively. The contribution of the added 1wt.% TiB_2 to Orowan precipitation strengthening in both the M-v250 and M-v550 samples was calculated to be 38.8 MPa. The total contribution of the Orowan precipitation strengthening in the P-v250, M-v250 and M-v550 samples were thus set to 83.2 MPa, 92 MPa and 108.2 MPa respectively.

4.2.4. Solid solution strengthening

Solid solution strengthening is mainly determined by the modulus mismatch and lattice mismatch between solute atoms and solvent atoms to hinder the movement of dislocations. Due to the large difference in atomic radii between Sn (1.4 Å) and Cu (1.28 Å) / Ni (1.24 Å), the solid solution strengthening in Cu15Ni8Sn in general is mainly caused by the dissolution of Sn [15,65], which may be expressed as follows [58,66]:

$$\sigma_{SS} = \frac{MG}{700}\varepsilon_{ss}^{3/2}c^{1/2} \quad (6)$$

$$\varepsilon_{SS} = \left|\varepsilon_G^{'} - \beta\varepsilon_b\right| \quad (7)$$

$$\varepsilon_G^{'} = \frac{\varepsilon_G}{1+\frac{1}{2}\left|\varepsilon_G\right|} \quad (8)$$

$$\varepsilon_G = \frac{1}{G}\frac{\mathrm{d}G}{\mathrm{d}c} \quad (9)$$

$$\varepsilon_b = \frac{1}{a}\frac{da}{dc} \quad (10)$$

where c is the concentration (at%) of the solute atom, β is a geometric parameter (taken as 3) and a is the lattice parameter of α-Cu based on previous studies [15,45,58]. The proportion of solid solution strengthening contributions is quite limited, so a value of 25 MPa from the literature [58] was used as the contribution of solid solution strengthening towards the three LPBF-

fabricated samples.

4.2.5. Load transfer strengthening

Compared to the LPBF-fabricated pure Cu15Ni8Sn samples, good particle-particle metallurgical bonding between the TiB_2 particles and the Cu15Ni8Sn matrix was found to have formed in the TiB_2-modified specimens. The load-bearing strengthening thus played an important role in the TiB_2-modified specimens. The contribution may be expressed as follows [67]:

$$\sigma_{LT} = \frac{3}{2} V_p \sigma_m \quad (11)$$

where σ_m is the yield strength of the Cu15Ni8Sn matrix (402 MPa) and V_p is the volume fraction of the reinforcing particles. The contribution of particle load-bearing strengthening to the modified Cu15Ni8Sn was determined to be 6.03 MPa.

The total yield strength of both Cu15Ni8Sn-pure and Cu15Ni8Sn-1wt.% TiB_2 samples fabricated via LPBF may be estimated by the root mean square combination of the above strengthening mechanism [68]:

$$\sigma_{CAL} = \sigma_0 + \sqrt{\sigma_{GBS}^2 + \sigma_{DIS}^2 + \sigma_{OPS}^2 + \sigma_{SS}^2 + \sigma_{LT}^2}$$

(Note that σ_{LT} for the pure sample is 0, and σ_0 is the lattice friction stress of Cu, which is taken as 52 MPa [15,60].) According to the above σ_{CAL} model, the yield strength temperatures of the three samples at room temperature were calculated, as shown in Fig. 14. The calculated yield strength values of the P-v250, M-v250 and M-v550 samples were determined to be 457.25 MPa, 390.15 MPa and 451.11 MPa, respectively. The experimentally obtained yield strength values of the three samples were determined to be 402 MPa, 396 MPa and 448 MPa, respectively. The calculation value of the TiB_2-modified material showed good agreement with the experimental results. The calculated yield strength of pure Cu15Ni8Sn was slightly higher than the experimental value. This deviation might be attributed to several factors, such as the regional locality of the precipitates, the calculation of grain size and the existence of metallurgical

defects [15].

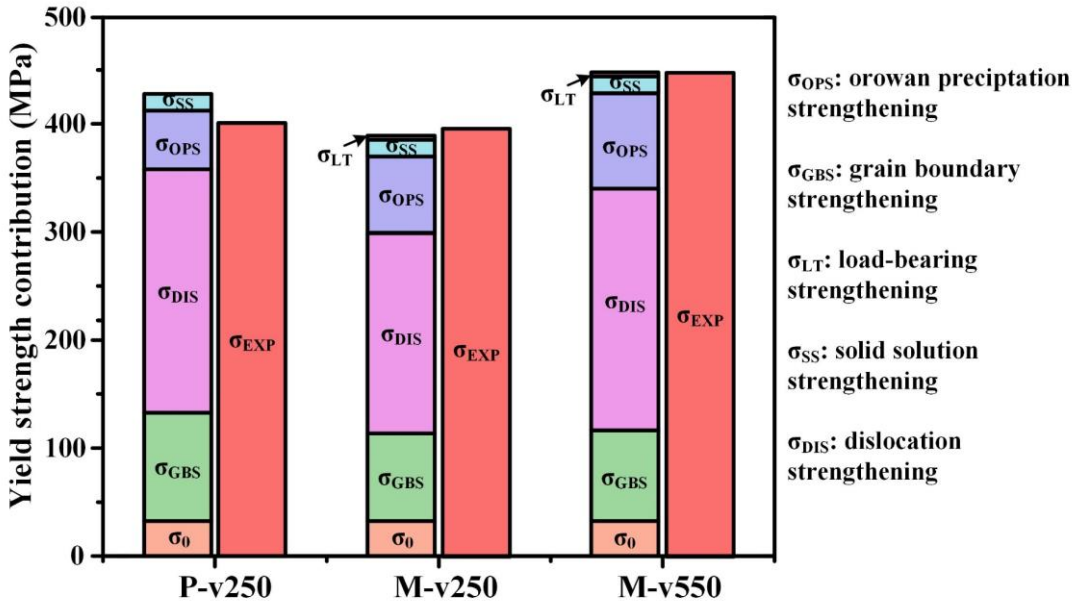

Fig. 14. The calculated and experimentally obtained strengthening contributions of the Cu15Ni8Sn-pure (P-v250) and Cu15Ni8Sn-1wt.% TiB_2 (M-v250 and M-v550) samples.

In addition, from the contribution of each strengthening mechanism shown in Fig. 14 to the overall calculated strength, the dislocation strengthening and grain boundary strengthening mechanisms played a leading role in strengthening the LPBF-fabricated pure Cu15Ni8Sn specimens. In addition to the dislocation strengthening and grain boundary strengthening mechanisms, the Orowan precipitation strengthening also played an important role in the TiB_2-modified Cu15Ni8Sn due to the second phase of TiB_2 ceramic particles. Note that the contribution of dislocation strengthening in M-v250 was about 50 MPa lower than that of the M-v550 sample, which explains the decrease in the yield strength of the M-v250 sample in the experimentally obtained stress-strain curve.

5. Conclusions

In this study, we have investigated the effects of added 1wt.% TiB_2 particles on processability during the laser powder bed fusion (LPBF) of Cu15Ni8Sn alloy.

The strengthening mechanisms within the LPBF of Cu15Ni8Sn-pure and 1wt.% TiB_2-modified Cu15Ni8Sn were also systematically analyzed. The following conclusions may be drawn from this study:

1. The processability improvement in the LPBF of TiB_2-modified Cu15Ni8Sn material was found to have been induced by the improvement in laser absorbability. The required optimal energy density was reduced to achieve nearly full-dense specimens without apparent pores and unmelted particles for the modified material compared to the original Cu15Ni8Sn.

2. The addition of TiB_2 particles was found to reduce the Sn-segregation behaviour in the as-fabricated Cu15Ni8Sn materials, implying that the size of the segregated phase may be tailored by the suitable selection of LPBF-process parameters. Grain refinement, however, was not found to have occurred during the LPBF of TiB_2-modified Cu15Ni8Sn, since the average equivalent grain size was 7 μm compared to 4.9 μm for the pure Cu15Ni8Sn.

3. Although grain refinement was not found to have occurred in the LPBF-fabricated TiB_2-modified Cu15Ni8Sn, the added 1 wt.% TiB_2 particles contributed to improvements in mechanical performance. The ultimate tensile strength value for pure Cu15Ni8Sn was measured to be 524 MPa, while the value increased to 601 MPa for the TiB_2-modified Cu15Ni8Sn, with no significant scarification in ductility.

4. The primary strengthening mechanisms for the LPBF-fabricated pure Cu15Ni8Sn used in this study included dislocation strengthening and grain boundary strengthening. Orowan precipitation strengthening also played a significant role in the Cu15Ni8Sn-1wt.% TiB_2 material, as did dislocation strengthening and grain boundary strengthening.

Data Availability

The raw/processed data required to reproduce these findings cannot be shared at this time as the data also forms part of an on-going study.

CRediT authorship contribution statement

Jian Gao: Conceptualization, Methodology, Writing – original draft. **Quanquan Han:** Conceptualization, Investigation, Writing – original draft, Funding acquisition. **Liqiao Wang:** Resources, Writing – review & editing. **Zhongyi Liu:** Visualization, Data curation. **Shwe Soe:** Writing – review & editing. **Zhenhua Zhang:** Investigation. **Yuchen Gu:** Methodology, Writing – review & editing.

Declaration of Competing Interest

The authors declare that they have no known competing financial interests or personal relationships that could have appeared to influence the work reported in this paper.

Acknowledgements

The authors appreciate the financial support from the National Natural Science Foundation of China (Grant No. 52005295), the State Key Laboratory of Materials Processing and Die & Mould Technology, Huazhong University of Science and Technology (Grant No. P2022-013), and the Key Laboratory of High-efficiency and Clean Mechanical Manufacture at Shandong University, Ministry of Education.

References

[1] L. Thijs, F. Verhaeghe, T. Craeghs, J. Van Humbeeck, J.P. Kruth, A study of the microstructural evolution during selective laser melting of Ti–6Al–4V, Acta Mater. 58 (2010) 3303–3312. https://doi.org/10.1016/J.ACTAMAT.2010.02.004.

[2] Q. Han, K.W.Q. Low, Y. Gu, X. Wang, L. Wang, B. Song, C. Huang, R. Setchi, The dynamics of reinforced particle migration in laser powder bed fusion of Ni-based composite, Powder Technol. 394 (2021) 714–723. https://doi.org/10.1016/J.POWTEC.2021.09.005.

[3] Q. Han, R. Mertens, M.L. Montero-Sistiaga, S. Yang, R. Setchi, K. Vanmeensel, B. Van Hooreweder, S.L. Evans, H. Fan, Laser powder bed fusion of Hastelloy X: Effects of hot isostatic pressing and the hot cracking mechanism, Mater. Sci. Eng. A. 732 (2018) 228–239. https://doi.org/10.1016/j.msea.2018.07.008.

[4] A.M. Khorasani, I. Gibson, U.S. Awan, A. Ghaderi, The effect of SLM process parameters on density, hardness, tensile strength and surface quality of Ti-6Al-4V, Addit. Manuf. 25 (2019) 176–186. https://doi.org/10.1016/J.ADDMA.2018.09.002.

[5] D. Gu, Y.C. Hagedorn, W. Meiners, K. Wissenbach, R. Poprawe, Nanocrystalline TiC reinforced Ti matrix bulk-form nanocomposites by Selective Laser Melting (SLM): Densification, growth

mechanism and wear behavior, Compos. Sci. Technol. 71 (2011) 1612–1620. https://doi.org/10.1016/J.COMPSCITECH.2011.07.010.

[6] Q. Han, R. Setchi, F. Lacan, D. Gu, S.L. Evans, Selective laser melting of advanced Al-Al2O3 nanocomposites: Simulation, microstructure and mechanical properties, Mater. Sci. Eng. A. 698 (2017) 162–173. https://doi.org/10.1016/j.msea.2017.05.061.

[7] R. Wang, L. Xi, K. Ding, B. Gökce, S. Barcikowski, D. Gu, Powder preparation during ball milling and laser additive manufacturing of aluminum matrix nanocomposites: Powder properties, processability and mechanical property, Adv. Powder Technol. 33 (2022) 103687. https://doi.org/10.1016/J.APT.2022.103687.

[8] Q. Han, Y. Gu, R. Setchi, F. Lacan, R. Johnston, S.L. Evans, S. Yang, Additive manufacturing of high-strength crack-free Ni-based Hastelloy X superalloy, Hast. Manuf. 30 (2019) 100919. https://doi.org/10.1016/j.addma.2019.100919.

[9] Q. Han, Y. Gu, J. Huang, L. Wang, K.W.Q. Low, Q. Feng, Y. Yin, R. Setchi, Selective laser melting of Hastelloy X nanocomposite: Effects of TiC reinforcement on crack elimination and strength improvement, Compos. Part B Eng. 202 (2020) 108442. https://doi.org/10.1016/J.COMPOSITESB.2020.108442.

[10] Y. Yin, J. Zhang, J. Gao, Z. Zhang, Q. Han, Z. Zan, Laser powder bed fusion of Ni-based Hastelloy X superalloy: Microstructure, anisotropic mechanical properties and strengthening mechanisms, Mater. Sci. Eng. A. 827 (2021) 142076. https://doi.org/10.1016/J.MSEA.2021.142076.

[11] X. Yan, C. Chang, D. Dong, S. Gao, W. Ma, M. Liu, H. Liao, S. Yin, Microstructure and mechanical properties of pure copper manufactured by selective laser melting, Mater. Sci. Eng. A. 789 (2020) 139615. https://doi.org/10.1016/J.MSEA.2020.139615.

[12] Y. Bai, C. Zhao, Y. Zhang, J. Chen, H. Wang, Additively manufactured CuCrZr alloy: Microstructure, mechanical properties and machinability, Mater. Sci. Eng. A. 819 (2021) 141528. https://doi.org/10.1016/j.msea.2021.141528.

[13] Z. Mao, D.Z. Zhang, J. Jiang, G. Fu, P. Zhang, Processing optimisation, mechanical properties and microstructural evolution during selective laser melting of Cu-15Sn high-tin bronze, Mater. Sci. Eng. A. 721 (2018) 125–134. https://doi.org/10.1016/J.MSEA.2018.02.051.

[14] G. Zhang, C. Chen, X. Wang, P. Wang, X. Zhang, X. Gan, K. Zhou, Additive manufacturing of fine-structured copper alloy by selective laser melting of pre-alloyed Cu-15Ni-8Sn powder, Int. J. Adv. Manuf. Technol. 96 (2018) 4223–4230. https://doi.org/10.1007/s00170-018-1891-3.

[15] J. Li, T. Cheng, Y. Liu, Y. Yang, W. Li, Q. Wei, Simultaneously enhanced strength and ductility of Cu-15Ni-8Sn alloy with periodic heterogeneous microstructures fabricated by laser powder bed fusion, Addit. Manuf. 54 (2022) 102726. https://doi.org/10.1016/J.ADDMA.2022.102726.

[16] N. Wang, Y. Shen, Q. An, K.M. Reddy, M. Jin, R. Karre, X. Wang, Microstructure evolution and mechanical property of Cu-15Ni-8Sn-0.2Nb alloy during aging treatment, J. Mater. Sci. Technol. 86 (2021) 227–236. https://doi.org/10.1016/J.JMST.2021.01.034.

[17] Z. Guo, J. Jie, S. Liu, Y. Zhang, B. Qin, T. Wang, T. Li, Effect of V addition on microstructures and mechanical properties of Cu-15Ni-8Sn alloy, Mater. Sci. Eng. A. 748 (2019) 85–94. https://doi.org/10.1016/J.MSEA.2019.01.084.

[18] M. Gao, Z. Chen, H. Kang, R. Li, W. Wang, C. Zou, T. Wang, Effects of Nb addition on the microstructures and mechanical properties of a precipitation hardening Cu-9Ni-6Sn alloy, Mater. Sci. Eng. A. 715 (2018) 340–347. https://doi.org/10.1016/J.MSEA.2018.01.022.

[19] T. DebRoy, T. Mukherjee, H.L. Wei, J.W. Elmer, J.O. Milewski, Metallurgy, mechanistic models and machine learning in metal printing, Nat. Rev. Mater. 6 (2021) 48–68. https://doi.org/10.1038/s41578-020-00236-1.

[20] S.D. Jadhav, S. Dadbakhsh, L. Goossens, J.P. Kruth, J. Van Humbeeck, K. Vanmeensel, Influence of selective laser melting process parameters on texture evolution in pure copper, J. Mater. Process. Technol. 270 (2019) 47–58. https://doi.org/10.1016/J.JMATPROTEC.2019.02.022.

[21] Y. Liu, J. Zhang, Q. Tan, Y. Yin, S. Liu, M. Li, M. Li, Q. Liu, Y. Zhou, T. Wu, F. Wang, M.X. Zhang, Additive manufacturing of high strength copper alloy with heterogeneous grain structure through laser powder bed fusion, Acta Mater. 220 (2021) 117311. https://doi.org/10.1016/J.ACTAMAT.2021.117311.

[22] J. Robinson, A. Arjunan, M. Stanford, I. Lyall, C. Williams, Effect of silver addition in copper-silver alloys fabricated by laser powder bed fusion in situ alloying, J. Alloys Compd. 857 (2021) 157561. https://doi.org/10.1016/J.JALLCOM.2020.157561.

[23] S.D. Jadhav, P.P. Dhekne, S. Dadbakhsh, J.P. Kruth, J. Van Humbeeck, K. Vanmeensel, Surface Modified Copper Alloy Powder for Reliable Laser-based Additive Manufacturing, Addit. Manuf. 35 (2020) 101418. https://doi.org/10.1016/J.ADDMA.2020.101418.

[24] B. Basu, G.B. Raju, A.K. Suri, Processing and properties of monolithic TiB2 based materials, Int. Mater. Rev. 51 (2006) 352–374. https://doi.org/10.1179/174328006X102529.

[25] Z. Feng, H. Tan, Y. Fang, X. Lin, W. Huang, Selective laser melting of TiB2/AlSi10Mg composite: Processability, microstructure and fracture behavior, J. Mater. Process. Technol. 299 (2022) 117386. https://doi.org/10.1016/J.JMATPROTEC.2021.117386.

[26] S. Yang, Q. Han, Y. Yin, J. Gao, Z. Zhang, Y. Gu, K.W.Q. Low, Effects of micrometer-sized TiB2 on crack mitigation, mechanical and electrochemical performance of a Ni-based alloy fabricated by selective laser melting, Opt. Laser Technol. 142 (2021) 107240. https://doi.org/10.1016/J.OPTLASTEC.2021.107240.

[27] Z. Zhang, Q. Han, S. Yang, Y. Yin, J. Gao, R. Setchi, Laser powder bed fusion of advanced submicrometer TiB2 reinforced high-performance Ni-based composite, Mater. Sci. Eng. A. 817 (2021) 141416. https://doi.org/10.1016/J.MSEA.2021.141416.

[28] J. Wang, X.L. Zhou, J. Li, M. Brochu, Y.F. Zhao, Microstructures and properties of SLM-manufactured Cu-15Ni-8Sn alloy, Addit. Manuf. 31 (2020) 100921. https://doi.org/10.1016/J.ADDMA.2019.100921.

[29] V.D. Divya, R. Muñoz-Moreno, O.M.D.M. Messé, J.S. Barnard, S. Baker, T. Illston, H.J. Stone, Microstructure of selective laser melted CM247LC nickel-based superalloy and its evolution through heat treatment, Mater. Charact. 114 (2016) 62–74. https://doi.org/10.1016/J.MATCHAR.2016.02.004.

[30] Q. Han, Y. Gu, L. Wang, Q. Feng, H. Gu, R. Johnston, R. Setchi, Effects of TiC content on microstructure and mechanical properties of nickel-based hastelloy X nanocomposites manufactured by selective laser melting, Mater. Sci. Eng. A. 796 (2020) 140008. https://doi.org/10.1016/j.msea.2020.140008.

[31] Q. Han, Y. Gu, J. Huang, L. Wang, K.W.Q. Low, Q. Feng, Y. Yin, R. Setchi, Selective laser melting of Hastelloy X nanocomposite: Effects of TiC reinforcement on crack elimination and strength improvement, Compos. Part B Eng. 202 (2020) 108442. https://doi.org/10.1016/j.compositesb.2020.108442.

[32] C. Ma, J. Zhao, C. Cao, T.C. Lin, X. Li, Fundamental study on laser interactions with

nanoparticles-reinforced metals-part II: Effect of nanoparticles on surface tension, viscosity, and laser melting, J. Manuf. Sci. Eng. Trans. ASME. 138 (2016) 2–7. https://doi.org/10.1115/1.4033446.

[33] D. Dai, D. Gu, Tailoring surface quality through mass and momentum transfer modeling using a volume of fluid method in selective laser melting of TiC/AlSi10Mg powder, Int. J. Mach. Tools Manuf. 88 (2015) 95–107. https://doi.org/10.1016/J.IJMACHTOOLS.2014.09.010.

[34] C.G. Pope, X-ray diffraction and the bragg equation, J. Chem. Educ. 74 (1997) 129–131. https://doi.org/10.1021/ed074p129.

[35] D. Gu, H. Zhang, D. Dai, M. Xia, C. Hong, R. Poprawe, Laser additive manufacturing of nano-TiC reinforced Ni-based nanocomposites with tailored microstructure and performance, Compos. Part B Eng. 163 (2019) 585–597. https://doi.org/10.1016/J.COMPOSITESB.2018.12.146.

[36] D. Zhang, Z. Feng, C. Wang, W. Wang, Z. Liu, W. Niu, Comparison of microstructures and mechanical properties of Inconel 718 alloy processed by selective laser melting and casting, Mater. Sci. Eng. A. 724 (2018) 357–367. https://doi.org/10.1016/J.MSEA.2018.03.073.

[37] L. Xi, P. Wang, K.G. Prashanth, H. Li, H. V. Prykhodko, S. Scudino, I. Kaban, Effect of TiB2 particles on microstructure and crystallographic texture of Al-12Si fabricated by selective laser melting, J. Alloys Compd. 786 (2019) 551–556. https://doi.org/10.1016/J.JALLCOM.2019.01.327.

[38] P. WANG, J. ECKERT, K. gokuldoss PRASHANTH, M. wei WU, I. KABAN, L. xia XI, S. SCUDINO, A review of particulate-reinforced aluminum matrix composites fabricated by selective laser melting, Trans. Nonferrous Met. Soc. China. 30 (2020) 2001–2034. https://doi.org/10.1016/S1003-6326(20)65357-2.

[39] Z. Zhang, Q. Han, Z. Liu, X. Wang, L. Wang, X. Yang, T. Ma, Z. Gao, Influence of the TiB2 content on the processability, microstructure and high-temperature tensile performance of a Ni-based superalloy by laser powder bed fusion, J. Alloys Compd. 908 (2022) 164656. https://doi.org/10.1016/J.JALLCOM.2022.164656.

[40] J.M. Park, E.S. Kim, H. Kwon, P. Sathiyamoorthi, K.T. Kim, J.H. Yu, H.S. Kim, Effect of heat treatment on microstructural heterogeneity and mechanical properties of 1%C-CoCrFeMnNi alloy fabricated by selective laser melting, Addit. Manuf. 47 (2021) 102283. https://doi.org/10.1016/J.ADDMA.2021.102283.

[41] X. Luo, D.D. Li, C. Yang, A. Gebert, H.Z. Lu, T. Song, H.W. Ma, L.M. Kang, Y. Long, Y.Y. Li, Circumventing the strength–ductility trade-off of β-type titanium alloys by defect engineering during laser powder bed fusion, Addit. Manuf. 51 (2022) 102640. https://doi.org/10.1016/J.ADDMA.2022.102640.

[42] Y. Liu, Y. Yang, D. Wang, A study on the residual stress during selective laser melting (SLM) of metallic powder, Int. J. Adv. Manuf. Technol. 87 (2016) 647–656. https://doi.org/10.1007/s00170-016-8466-y.

[43] B. Cheng, S. Shrestha, K. Chou, Stress and deformation evaluations of scanning strategy effect in selective laser melting, Addit. Manuf. 12 (2016) 240–251. https://doi.org/10.1016/J.ADDMA.2016.05.007.

[44] H. Zhang, D. Gu, C. Ma, M. Guo, J. Yang, H. Zhang, H. Chen, C. Li, K. Svynarenko, K. Kosiba, Understanding tensile and creep properties of WC reinforced nickel-based composites fabricated by selective laser melting, Mater. Sci. Eng. A. 802 (2021) 140431. https://doi.org/10.1016/J.MSEA.2020.140431.

[45] G. Zhang, S. Liu, C. Chen, X. Zhang, X. Gan, Q. Lei, Z. Li, K. Zhou, Effect of heat treatment on microstructure and mechanical properties of a selective laser melted Cu–15Ni–8Sn alloy, Mater. Sci. Eng. A. 763 (2019) 138132. https://doi.org/10.1016/J.MSEA.2019.138132.

[46] P. Köhnen, M. Létang, M. Voshage, J.H. Schleifenbaum, C. Haase, Understanding the process-microstructure correlations for tailoring the mechanical properties of L-PBF produced austenitic advanced high strength steel, Addit. Manuf. 30 (2019) 100914. https://doi.org/10.1016/J.ADDMA.2019.100914.

[47] Y.L. Kuo, A. Kamigaichi, K. Kakehi, Characterization of Ni-Based Superalloy Built by Selective Laser Melting and Electron Beam Melting, Metall. Mater. Trans. A Phys. Metall. Mater. Sci. 49 (2018) 3831–3837. https://doi.org/10.1007/s11661-018-4769-y.

[48] Z. Ma, K. Zhang, Z. Ren, D.Z. Zhang, G. Tao, H. Xu, Selective laser melting of Cu–Cr–Zr copper alloy: Parameter optimization, microstructure and mechanical properties, J. Alloys Compd. 828 (2020) 154350. https://doi.org/10.1016/J.JALLCOM.2020.154350.

[49] Y.K. Xiao, Z.Y. Bian, Y. Wu, G. Ji, Y.Q. Li, M.J. Li, Q. Lian, Z. Chen, A. Addad, H.W. Wang, Effect of nano-TiB2 particles on the anisotropy in an AlSi10Mg alloy processed by selective laser melting, J. Alloys Compd. 798 (2019) 644–655. https://doi.org/10.1016/J.JALLCOM.2019.05.279.

[50] Y.K. Kim, J.H. Yu, H.S. Kim, K.A. Lee, In-situ carbide-reinforced CoCrFeMnNi high-entropy alloy matrix nanocomposites manufactured by selective laser melting: Carbon content effects on microstructure, mechanical properties, and deformation mechanism, Compos. Part B Eng. 210 (2021) 108638. https://doi.org/10.1016/J.COMPOSITESB.2021.108638.

[51] Z. Wu, C.M. Parish, H. Bei, Nano-twin mediated plasticity in carbon-containing FeNiCoCrMn high entropy alloys, J. Alloys Compd. 647 (2015) 815–822. https://doi.org/10.1016/J.JALLCOM.2015.05.224.

[52] V.A. Popovich, E. V. Borisov, A.A. Popovich, V.S. Sufiiarov, D. V. Masaylo, L. Alzina, Functionally graded Inconel 718 processed by additive manufacturing: Crystallographic texture, anisotropy of microstructure and mechanical properties, Mater. Des. 114 (2017) 441–449. https://doi.org/10.1016/J.MATDES.2016.10.075.

[53] J. Wang, X. Zhou, J. Li, Evolution of microstructures and properties of SLM-manufactured Cu–15Ni–8Sn alloy during heat treatment, Addit. Manuf. 37 (2021) 101599. https://doi.org/10.1016/J.ADDMA.2020.101599.

[54] G. Peng, X. Gan, Y. Jiang, Z. Li, K. Zhou, Effect of dynamic strain aging on the deformation behavior and microstructure of Cu-15Ni-8Sn alloy, J. Alloys Compd. 718 (2017) 182–187. https://doi.org/10.1016/J.JALLCOM.2017.05.127.

[55] D. Jafari, W.W. Wits, T.H.J. Vaneker, A.G. Demir, B. Previtali, B.J. Geurts, I. Gibson, Pulsed mode selective laser melting of porous structures: Structural and thermophysical characterization, Addit. Manuf. 35 (2020) 101263. https://doi.org/10.1016/J.ADDMA.2020.101263.

[56] O. Popov, T. Avramenko, V. Vishnyakov, Thermal conductivity and thermal shock resistance of TiB2-basedUHTCs enhanced by graphite platelets, Mater. Today Commun. 26 (2021) 101756. https://doi.org/10.1016/J.MTCOMM.2020.101756.

[57] D.H. Yang, Y.K. Kim, S.H. Park, K.A. Lee, Improved mechanical and thermophysical properties of additively manufactured Cu-Ni-Sn-P alloy by using aging treatment, J. Alloys Compd. 875 (2021) 160050. https://doi.org/10.1016/J.JALLCOM.2021.160050.

[58] C. Zhao, Z. Wang, D. Li, L. Kollo, Z. Luo, W. Zhang, K.G. Prashanth, Selective laser melting of Cu–Ni–Sn: A comprehensive study on the microstructure, mechanical properties, and deformation behavior, Int. J. Plast. 138 (2021) 102926. https://doi.org/10.1016/J.IJPLAS.2021.102926.

[59] W.H. Yu, S.L. Sing, C.K. Chua, C.N. Kuo, X.L. Tian, Particle-reinforced metal matrix nanocomposites fabricated by selective laser melting: A state of the art review, Prog. Mater. Sci. 104 (2019) 330–379. https://doi.org/10.1016/J.PMATSCI.2019.04.006.

[60] Q. Lei, Z. Xiao, W. Hu, B. Derby, Z. Li, Phase transformation behaviors and properties of a high strength Cu-Ni-Si alloy, Mater. Sci. Eng. A. 697 (2017) 37–47. https://doi.org/10.1016/J.MSEA.2017.05.001.

[61] Y. Liu, Z. Li, Y. Jiang, Y. Zhang, Z. Zhou, Q. Lei, The microstructure evolution and properties of a Cu-Cr-Ag alloy during thermal-mechanical treatment, J. Mater. Res. 32 (2017) 1324–1332. https://doi.org/10.1557/jmr.2017.17.

[62] H. Cheng, H.Y. Wang, Y.C. Xie, Q.H. Tang, P.Q. Dai, Controllable fabrication of a carbide-containing FeCoCrNiMn high-entropy alloy: microstructure and mechanical properties, Mater. Sci. Technol. (United Kingdom). 33 (2017) 2032–2039. https://doi.org/10.1080/02670836.2017.1342367.

[63] M. Mabuchi, K. Higashi, Strengthening mechanisms of Mg□Si alloys, Acta Mater. 44 (1996) 4611–4618. https://doi.org/10.1016/1359-6454(96)00072-9.

[64] M. Mabuchi, K. Higashi, Strengthening mechanisms of Mg-Si alloys, Acta Mater. 44 (1996) 4611–4618. https://doi.org/10.1016/1359-6454(96)00072-9.

[65] J.C. Zhao, M.R. Notis, Spinodal decomposition, ordering transformation, and discontinuous precipitation in a Cu–15Ni–8Sn alloy, Acta Mater. 46 (1998) 4203–4218. https://doi.org/10.1016/S1359-6454(98)00095-0.

[66] H. Wen, T.D. Topping, D. Isheim, D.N. Seidman, E.J. Lavernia, Strengthening mechanisms in a high-strength bulk nanostructured Cu–Zn–Al alloy processed via cryomilling and spark plasma sintering, Acta Mater. 61 (2013) 2769–2782. https://doi.org/10.1016/J.ACTAMAT.2012.09.036.

[67] J. Wang, T. Liu, L. Luo, X. Cai, B. Wang, J. Zhao, Z. Cheng, L. Wang, Y. Su, X. Xue, J. Guo, Selective laser melting of high-strength TiB2/AlMgScZr composites: microstructure, tensile deformation behavior, and mechanical properties, J. Mater. Res. Technol. 16 (2022) 786–800. https://doi.org/10.1016/J.JMRT.2021.11.150.

[68] B. AlMangour, Y.K. Kim, D. Grzesiak, K.A. Lee, Novel TiB2-reinforced 316L stainless steel nanocomposites with excellent room- and high-temperature yield strength developed by additive manufacturing, Compos. Part B Eng. 156 (2019) 51–63. https://doi.org/10.1016/J.COMPOSITESB.2018.07.050.